Published in final edited form as:
J Inorg Biochem. 2008 February ; 102(2): 216–233. doi:10.1016/j.jinorgbio.2007.08.002.

Crystal Structures of Manganese- and Cobalt-substituted Myoglobin in Complex with NO and Nitrite Reveal Unusual Ligand Conformations

Zaki N. Zahran, **Lilian Chooback**, **Daniel M. Copeland**, **Ann H. West**, and **George B. Richter-Addo***
Department of Chemistry and Biochemistry, University of Oklahoma, 620 Parrington Oval, Norman, OK 73019

Abstract

Nitrite is now recognized as a storage pool of bioactive nitric oxide (NO). Hemoglobin (Hb) and myoglobin (Mb) convert, under certain conditions, nitrite to NO. This newly discovered nitrite reductase activity of Hb and Mb provides an attractive alternative to mammalian NO synthesis from the NO synthase pathway that requires dioxygen. We recently reported the X-ray crystal structure of the nitrite adduct of ferric horse heart Mb, and showed that the nitrite ligand binds in an unprecedented *O*-binding (nitrito) mode to the d^5 ferric center in $Mb^{III}(ONO)$ (D. M. Copeland, A. Soares, A. H. West, G. B. Richter-Addo, J. Inorg. Biochem. 100 (2006) 1413-1425). We also showed that the distal pocket in Mb allows for different conformations of the NO ligand (120° and 144°) in $Mb^{II}NO$ depending on the mode of preparation of the compound. In this article, we report the crystal structures of the nitrite and NO adducts of manganese-substituted hh Mb (a d^4 system) and of the nitrite adduct of cobalt-substituted hh Mb (a d^6 system). We show that the distal His64 residue directs the nitrite ligand towards the rare nitrito *O*-binding mode in $Mn^{III}Mb$ and $Co^{III}Mb$. We also report that the distal pocket residues allow a stabilization of an unprecendented bent MnNO moiety in $Mn^{II}MbNO$. These crystal structural data, when combined with the data for the aquo, methanol, and azide MnMb derivatives, provide information on the role of distal pocket residues in the observed binding modes of nitrite and NO ligands to wild-type and metal-substituted Mb.

Keywords

Nitrite; Nitric oxide; X-ray; Heme; Manganese; Cobalt; Myoglobin

1. Introduction

Nitrite (NO_2^-) is a simple oxyanion of nitrogen that has long been thought of as being a “dead end” product of nitric oxide (NO) metabolism. Exogenous nitrite can be harmful. A well-known consequence of nitrite poisoning is methemoglobinemia [1]. Nitrite can oxidize ferrous hemoglobin to its ferric form (metHb), and the increased *in vivo* level of metHb relative to the oxygen-binding ferrous form results in the reduced capacity of the total Hb to efficiently

* Corresponding author. Tel: +1 405 325 4812: fax +1 405 325 6111. grichteraddo@ou.edu (G. B. Richter-Addo).

Supplementary data: Figs. S1-S3 accompany this article.

transport dioxygen [1,2]. Common symptoms of methemoglobinemia are greyish cyanotic skin color (10-20% metHb), lethargy and headaches (20-50% metHb), seizures (50% metHb) and death (>70% metHb), although at least one patient with 68% or higher metHb due to nitrite poisoning survived [2].

The physiological role of nitrite is only now being fully recognized [3,4]. For example, infusion of nitrite into the forearm brachial artery results in increased blood flow in the forearm before and during exercise, suggesting a unique role of nitrite in vasodilation [5]. Pulmonary vasodilation by nitrite has been reported [6]. It has been known for some time that deoxyHb will convert nitrite to NO and ferric heme under anaerobic conditions [5,7,8]. This "enzymatic nitrite reductase" function of Hb, at first glance, is quite unexpected since most of the NO generated is then captured by deoxyHb to form a ferrous HbNO product. Gladwin and coworkers have recently reported a careful study of this nitrite reductase reaction using anaerobic and partially oxygenated solutions to demonstrate that the NO produced can be released as free NO under normal and hypoxic physiological conditions [9]. This nitrite reducase activity of Hb to produce NO under conditions of hypoxia thus essentially bypasses the dioxygen-dependent nitric oxide synthase pathway [3,10]. Further, the related reaction of deoxyMb with nitrite to produce NO has been shown to regulate mitochondrial respiration [11].

Manganese is an essential trace element that has one less electron than iron. Manganese-substituted derivatives of a number of heme proteins have been prepared and studied. In many cases, these Mn-substituted derivatives were investigated in order to provide insight on the role of heme iron in the reactions of the native proteins [12]. Manganese-substituted derivatives of heme proteins that have been reported to date include those of Hb [13,14], myoglobin (Mb) [15-17], cytochrome P450 [18], sGC [19], cytochrome *c* [20], nitric oxide synthase [21], horseradish peroxidase [14,16,22], cytochrome b_5 [23], C*c*P [16,24,25], and PGHS-1 [26].

It is interesting to note that nearly fifty years ago, Borg and Cotzias discovered that injection of radiolabeled $^{54}MnCl_2$ into patients *in vivo* resulted in the incorporation of Mn^{II} into red cell fractions, and that the incorporated Mn^{II} was non-exchangeable and non-dialyzable [27]. Based on their data, they suggested that the Mn^{II} was most likely incorporated into heme, thus providing some circumstantial evidence for the production of a natural manganese heme in humans [28]. Mahoney and Sargent confirmed this finding, and showed that between 0.5-9.0% of administered radiolabeled ^{54}Mn was incorporated into red blood cells, and that 60-70% of the radioactivity was recovered in the resulting crystalline hemin preparation [29]. Hancock and Fritze later showed that, indeed, injection of $^{54}MnCl_2$ into rats resulted in the formation of a ^{54}Mn-containing species that had identical gel chromatographic elution behavior as hemoglobin, bis-pyridine hemochrome, and hematin [30]; this provided further evidence for the *in vivo* formation of a manganese porphyrin, confirming the earlier results of Borg and Cotzias. These authors noted, however, that added Mn^{II} was not able to displace iron from heme by a simple metal displacement reaction, suggesting the incorporation of Mn^{II} at the heme biosynthesis stage. In a separate study, Wibowo *et al.* determined that increased levels of protoporphyrin in erythrocytes (induced by exposure to Pb) resulted in incorporation of *in vivo* manganese by the porphyrin [31]. In metal ion accumulation studies using Norway lobsters, it was determined that exposure of the lobsters to Mn^{II} resulted in accumulation of the metal ion in nerve tissue, and in the hemolymph where it was bound mainly to the respiratory protein hemocyanin (the authors noted that Mn^{II} was not able to displace copper in the protein) [32].

Unlike the native iron analogues, Mn^{II}-substituted Hb (Mn^{II}Hb) and –myoglobin (Mn^{II}Mb) *do not* bind dioxygen or carbon monoxide [16], although the Mn^{III}-derivatives bind azide

[16,33-35]. Mitra and coworkers have shown that $Mn^{III}Mb$ binds cyanide and thiocyanate at a location >6Å from the metal center [36].

Interestingly, Mn-substituted Hb (MnHb) exhibits allosteric effects in its binding of NO [34, 37-39]. The resulting adduct, written simply as $Mn^{II}HbNO$, has been prepared and characterized by spectroscopy [34,40,41]. The NO adduct of Mn-substituted Mb is also known [34,40], as are the NO adducts of Mn-substituted sGC [19], cytochrome *c* [20], C*c*P [40], cytochrome P450 [18], and that of a monomeric MnHb from the insect *Chironomus thummi thummi* [42]. Lan and coworkers have examined the ability of sol-gel encapsulated $Mn^{II}Mb$ to act as an NO sensor under physiological conditions (since it binds NO but not O_2) [43]. We, and others, have prepared and characterized several synthetic manganese porphyrins ((por)Mn) that bind NO [44-49]. In some cases, synthetic (por)Mn compounds have been shown to electrocatalyze the reduction of NO to hydroxylamine and ammonia [50].

Clearly, Mn porphyrins are becoming increasingly recognized for their potential applications. Despite numerous reports on the spectroscopy of Mn-substituted heme proteins, there are only a few reports of crystal structures of these complexes. Moffat and coworkers reported the structure of MnHb using X-ray difference Fourier techniques [51,52], and demonstrated the similarity of the structure of this complex to that of the native iron compound. Arnone later reported the 3.0 Å resolution structure of the heterometallic complex Hb(α-$Fe^{II}CO$)(β-Mn^{II}) [53]. Very recently, Loll and coworkers reported the 2.0 Å resolution crystal structure of Mn-PGHS [26]. To the best of our knowledge, despite the increased attention given to the potential biological activities of Mn-hemes, these are the only reported crystal structures of Mn-substituted heme proteins.

We are interested in the structures of the heme pockets in Mb derivatives of nitrogen oxides (NOx; x = 1, 2) and how the distal amino acid residues might affect the binding preferences of these NOx ligands. In this manuscript, we describe, for the first time, the crystal structures of Mn-substituted Mb and its NOx-liganded derivatives, and the crystal structure of the analogous cobalt-substituted Mb-nitrite compound. Cobalt-substituted heme proteins have also provided valuable information about the native systems. For example, Makino and coworkers showed that cobalt-substituted sGC is a functional enzyme that is responsive to NO [54]. The crystal structures reported here help explain some of the contradictory results on the spectroscopy previously reported in the literature.

2. Experimental

Manganese(III) protoporphyrin IX chloride ((PPIX)$Mn^{III}Cl$), sodium dithionite (85%), and 2-butanone were purchased from Aldrich Chemical Company. Tris(hydroxymethyl) aminomethane hydrochloride (Tris-HCl, molecular biology grade), and ammonium sulfate (99.5%) were obtained from Fluka. Sodium nitrite (98.0%) was obtained from Baker and Adamson. Cobalt(III) protoporphyrin IX chloride ((PPIX)$Co^{III}Cl$) was purchased from Frontier Scientific Company. Nitric oxide (98%, Matheson Gas) was passed through KOH pellets and two cold traps (dry ice/acetone, −78 °C) to remove higher nitrogen oxides.

Horse heart *met*-myoglobin (hh *met*Mb) was purchased from Sigma. The heme group was removed from *met*Mb (30 mg/ml) using the method of Yonetani [24] and Teale [55]. (PPIX)Mn^{III} was reconstituted into apoMb following the method of Yonetani [16], and the product characterized by UV-visible (UV-vis) spectroscopy (λ_{max} 378 and 471 nm) [16,17]. The $Co^{III}Mb$ complex was similarly prepared and characterized (λ_{max} 425 nm) [56]. The purity of the metal-reconstituted myoglobins were established by SDS PAGE.

2.1 Crystallization and complex formation

All eight Mn- and Co-substituted myoglobin crystalline complexes were prepared and structurally characterized in (at least) duplicate.

2.1.1. $Mn^{III}Mb$ and $Co^{III}Mb$—Crystals of $Mn^{III}Mb$ and $Co^{III}Mb$ were grown using identical procedures. The crystals were grown at room temperature (~23 °C) using the hanging-drop vapor diffusion method. A hanging drop (10 μL) containing 0.45 mM protein (8 mg/mL) and 0.8 M $(NH_4)_2SO_4$ in 10 mM Tris-HCl buffer at pH 7.4, was suspended over a well containing 500 μL of 3.4 M $(NH_4)_2SO_4$ in 10 mM Tris-HCl buffer at pH 7.4. The crystals grew in clusters of plates and reached a suitable size in 3-5 days. A suitable crystal was harvested with a cryoloop, transferred to 10 μL of artificial mother liquor containing 10% glycerol as a cryoprotectant, and flash frozen in liquid nitrogen.

2.1.2. $Mn^{III}Mb(ONO^{-})$—The nitrito-liganded complex, $Mn^{III}Mb(ONO^{-})$, was obtained by soaking crystals of $Mn^{III}Mb$ in a 10 μL droplet of the buffer (10 mM Tris-HCl, pH 7.4) under anaerobic conditions by submerging the droplet in mineral oil. The droplet contained $(NH_4)_2SO_4$ (3.4 M), 7.5% glycerol as cryoprotectant, sodium dithionite (187 mM). Sodium nitrite (to give 100 mM) was then added to the droplet, and the crystal soaked for 2 min in this mixture. The crystals were then harvested with cryoloops and flash frozen in liquid nitrogen. We note that in our hands, the $Mn^{III}Mb(ONO^{-})$ complex could not be obtained either by soaking the $Mn^{III}Mb$ crystals in a droplet free of sodium dithionite (but containing the other components), or from co-crystallization of $Mn^{III}Mb$ in presence of excess $NaNO_2$.

2.1.3. $Co^{III}Mb(ONO^{-})$—The $Co^{III}Mb(ONO^{-})$ complex was prepared by mixing a solution of $Co^{III}Mb$ (10 mg/mL) with a solution of $NaNO_2$ (0.5 M) in a 1:1 v/v ratio and keeping the mixture at 4 °C for 30 min. The product was then crystallized using the vapor diffusion method using the same conditions as used for $Co^{III}Mb(H_2O)$, and suitable size crystals grew in 3-5 days. Suitable crystals were harvested with cryoloops and flash frozen in liquid nitrogen. The complex was also obtained by soaking $Co^{III}Mb$ crystals in a droplet of Tris-HCl buffer (10 mM, pH 7.4) containing $(NH_4)_2SO_4$ (3.4 M), 10% glycerol as cryoprotectant, and $NaNO_2$ (500 mM) for 30 min. However, this latter method resulted in a product containing nitrite at only ~60 % occupancy as determined by crystallography.

2.1.4. $Mn^{II}Mb$—The reduced $Mn^{II}Mb$ crystal was obtained by soaking a crystal of $Mn^{III}Mb$ anaerobically in a 20 μL droplet of the buffer (10 mM Tris-HCl, pH 7.4) containing $(NH_4)_2SO_4$ (3.4 M), 10% glycerol as cryoprotectant, and sodium dithionite (114 mM) for at least 20 min. The crystal and the droplet were submerged in mineral oil under an atmosphere of nitrogen. During the soaking of the crystal, it cracked into several pieces and its color changed from purple-red to orange-red indicative of the formation of the reduced $Mn^{II}Mb$ [16,57]. A suitable crystal was harvested with a cryoloop and flash frozen in liquid nitrogen.

2.1.5. $Mn^{II}MbNO$—This complex was obtained by transferring a crystal of $Mn^{II}Mb$ into a 10 μL droplet of the buffer (10 mM Tris-HCl, pH 7.4) under anaerobic conditions and submerged in mineral oil. The droplet contained $(NH_4)_2SO_4$ (3.4 M), 10% glycerol as cryoprotectant, and NO (~2 mM). The crystal was soaked in this solution for ~2 min, and the color changed from orange-red to pink suggesting formation of the nitrosyl adduct $Mn^{II}MbNO$. The crystal was harvested with a cryoloop and flash frozen in liquid nitrogen.

2.1.6. $Mn^{III}Mb(MeOH)$—The $Mn^{III}Mb(MeOH)$ complex was prepared by adding 20 μL MeOH to a $Mn^{III}Mb$ solution (180 μL, 0.9 mM) in 10 mM Tris-HCl buffer at pH 7.4. The mixture was kept at 4°C for 10 min before setting up for crystallization using the hanging drop vapor diffusion method employing the same conditions as described above for $Mn^{III}Mb$. A

suitable crystal was harvested and soaked for 10 min in a droplet of 10 mM Tris-HCl buffer (pH 7.4) containing $(NH_4)_2SO_4$ (3.4 M), 10% glycerol as cryoprotectant, and MeOH (2% v/v). The crystal was then flash frozen in liquid nitrogen.

2.1.7. $Mb^{III}Mb(N_3^-)$—The azide complex was prepared as reported previously [35,58] by adding 20 μL of a sodium azide solution (200 mM) directly into a solution of $Mn^{III}Mb$ (180 μL, 0.9 mM) in 10 mM Tris-HCl buffer at pH 7.4. The mixture was left at 4 °C for 10 min, and the resulting azide complex crystallized using the hanging-drop vapor diffusion method employing the same conditions as described above for $Mn^{III}Mb$. Crystals grew in 3-5 days. A suitable crystal was harvested and soaked in a 10 μL droplet of 10 mM Tris-HCl buffer (pH 7.4) containing $(NH_4)_2SO_4$ (3.4 M), 10% glycerol as cryoprotectant, and NaN_3 (200 mM) for 10 min, and flash frozen in liquid nitrogen. The excess NaN_3 added to the cryoprotectant was to maximize the occupancy of the azide ligand in the complex.

2.2. X-ray diffraction data collection and processing

Diffraction data sets were collected at 100 K by using CuKα radiation (λ = 1.5418 Å) produced from a RigakuMSC RU-H3R X-ray generator operated at 50 kV/100 mA. Diffracted X-rays were detected using an R-AXIS IV^{++} dual image plate detector system. The crystal-to-detector distance was set at 100 mm, and 220 frames of data were collected for each crystal, with 1° oscillations and a 5 min exposure time per frame. X-ray intensity data were indexed and processed with the stand-alone *d*TREK* program (Macintosh v.2D) [59] available from Molecular Structure Corporation.

2.3. Structure Solution and Refinement

The CCP4 Suite of programs [60] was used for structure solution and the subsequent refinement of all structures reported here. Phase information was obtained using molecular replacement as implemented in CCP4 (*MOLREP*) [61]. The search model was the 1.3 Å resolution structure of $Mb^{II}NO$ (PDB access code 2FRJ) [62] with all the solvent molecules, sulfate anions, and the NO ligand removed from the structure. After molecular replacement, the iron atom was replaced by manganese or cobalt, and restrained refinement was performed for all atoms. However, there were no restraints placed on the axial metal-ligand or metal-N(His93) bond distances or angles. In all the structures, no electron density was observed for the C-terminal residue Gly153, thus it was not included in the models. In all cases, *ARP*/*wARP* was used to add water molecules to the structure during refinement. Lys47 was refined in two positions at 50% occupancy each. Also, two sulfate groups (three in case of reduced $Mn^{II}Mb$) were added to the models based on the initial F_o-F_c map. After completion of the refinement of the individual structures, the interactive macromolecular structure validation tool *MolPROBITY* (available online from the Richardson Lab at Duke University at http://kinemage.biochem.duke.edu/molprobity/) [63,64] was utilized to assign the final rotamer orientations of Asn, Gln, and His side chains, and to test for any unusual side chain contacts.

In general, the structure solution and refinement procedures were similar for all eight structures reported here. The statistics of the data collection and refinement are summarized in Table 1. Selected geometrical data, calculated using SHELXTL v5.1, are presented in Table 2. The F_o-F_c difference electron density maps shown in Figs. 1 and 2 were generated using *CNS* [65], and F_cs were calculated using the final model but by omitting the ligand from the structure. All figures were drawn using *PyMOL* (Delano Scientific, 2002; http//www.pymol.org) and labels added using Adobe® Photoshop.

2.3.1. $Mn^{III}Mb(H_2O)$—After molecular replacement, the *R*-factor was 30.98%. After 10 cycles of restrained refinement, the *R*-factor was 24.86% and initial electron density maps were

generated. At this stage, the initial F_o-F_c difference electron density map revealed the presence of cone-shaped electron density in the distal Mn-heme pocket. We initially tried to model this as a methanol molecule (see Results Section). This cone-shaped electron density was finally refined as a single water molecule in two disordered positions with 70% and 30% occupancies. Two conformations of the distal His64 residue were modeled into the electron density, and the occupancies refined to 70% and 30%. Solvent water molecules were added, followed by an additional 15 cycles of refinement with *B*-factors refined anisotropically, and the *R*-factor dropped to 17.9%.

2.3.2. $Mn^{III}Mb(ONO^-)$—At the start of refinement, the *R*-factor was 32.11%. After 15 cycles of restrained refinement, the *R*-factor dropped to 24.36%. The F_o-F_c difference electron density map showed clear density for the nitrite ligand in the Mn-heme distal pocket, and nitrite was modeled into the density. After the addition of solvent molecules and further cycles of refinement, the *R*-factor dropped to 18.6%.

2.3.3. $Co^{III}Mb(H_2O)$—After molecular replacement, the *R*-factor was 33.50%. After 10 cycles of restrained refinement, the *R*-factor dropped to 24.38%. The F_o-F_c difference electron density map showed the presence of electron density consistent with the presence of a bound water molecule (bound to the heme cobalt atom). After the addition of solvent molecules and further cycles of refinement, the *R*-factor dropped to 19.3%.

2.3.4. $Co^{III}Mb(ONO^-)$—After molecular replacement, the *R*-factor was 30.52%. After 10 cycles of restrained refinement, the *R*-factor dropped to 24.49%. The F_o-F_c difference electron density map showed clear density for the nitrite ligand in the Co-heme distal pocket, and nitrite was modeled into the density. After the addition of solvent molecules and further cycles of refinement, the final *R*-factor dropped to 17.4%.

2.3.5. $Mn^{II}Mb$—After molecular replacement, the *R*-factor was 33.09%. After 10 cycles of restrained refinement the *R*-factor dropped to 22.09% and the initial F_o-F_c difference electron density map showed the absence of electron density for any ligand in the Mn-heme distal pocket. After the addition of the water molecules and further cycles of refinement, the *R*-factor dropped to 19.4%.

2.3.6. $Mn^{II}Mb(NO)$—At the start of refinement, the *R*-factor was 30.77%. After 10 cycles of restrained refinement, the *R*-factor dropped to 22.23%. The F_o-F_c difference electron density map showed clear density for the nitrosyl ligand in the Mn-heme distal pocket, and NO was modeled into the density. After the addition of solvent molecules and further cycles of refinement, the final *R*-factor dropped to 17.7%. The NO ligand refined to 70% occupancy. Two conformations of the distal His64 were modeled into the electron density associated with this residue, and were refined with 70% and 30% occupancies.

2.3.7. $Mn^{III}Mb(MeOH)$—At the start of refinement, the *R*-factor was 28.79%. After 10 cycles of restrained refinement, the *R*-factor dropped to 22.74% and initial electron density maps were generated. The F_o-F_c difference electron density map showed clear electron density for the methanol ligand in the Mn-heme distal pocket, and methanol was modeled into this density. After the addition of solvent molecules and further cycles of refinement, the *R*-factor dropped to 17.4%. The methanol ligand refined to full occupancy with thermal factors of 14.25 and 11.69 $Å^2$ for its O and C atoms, respectively.

2.3.8. $Mn^{III}Mb(N_3^-)$—After molecular replacement, the *R*-factor was 31.52%. Ten cycles of restrained refinement resulted in the lowering of the *R*-factor to 24.93%. The F_o-F_c difference electron density map showed clear density for the azide ligand in the Mn-heme distal pocket,

and azide was modeled into the density. Solvent molecules were added, and further cycles of refinement dropped the *R*-factor to 18.4 %. The azide ligand refined to near-full (94%) occupancy, with thermal factors of 17.95, 20.28 and 22.17 $Å^2$ for its N1, N2, and N3 atoms, respectively.

2.4. Protein Data Bank accession numbers

Atomic coordinates and structure factor amplitudes have been deposited with the RCSB Protein Data Bank. The accession codes are listed in Table 1.

3. Results

The crystal structures of the Mn- and Co-substituted myoglobin derivatives reported here display the normal fold expected for the native horse heart myoglobin. The differences lie in the nature of the heme axial ligand and the resulting distal pocket structure. Hence, we focus on the heme environment in these complexes, and selected structural data are shown in Table 2.

The crystal structure of the parent Mn-substituted myoglobin had not been reported prior to this study. Further, the crystal structures of the derivatives reported here were obtained by derivatizing crystals of the parent Mn-substituted myoglobin. Hence, it was important that we determined its crystal structure.

3.1. $Mn^{III}Mb(H_2O)$

The Mn^{III}-reconstituted myoglobin (Mn^{III}Mb) was prepared from the reaction of Mn^{III}-protoporphyrin IX chloride and apo-Mb in solution, and its formation confirmed by UV-vis spectroscopy. The compound in solution displays a characteristic split Soret absorption at 378 and 471 nm as reported by Yonetani *et al.* [24]. We determined the crystal structure of this complex to 1.65 Å resolution. The Mn^{III}-heme environment is shown in Fig. 1a. We also show the final F_o-F_c difference electron density map, contoured at 3σ, that reveals the presence of the axial water ligand. This axial water is best refined as a disordered molecule in two distinct positions, with 70% (coordinated) and 30% (uncoordinated) occupancies. We located two positions for the distal His64 residue, and the occupancies correlate with the two water molecule positions. The $2F_o$-F_c map showing the electron density associated with the two His64 conformations is shown in Fig. S1 in the Supplementary Information. The distance between the N^{ε} atoms of the two His64 conformations is 0.74 Å, with the minor conformation closer to the interior of the protein and closer to the uncoordinated water molecule.

The major disordered position of the water ligand is close to the Mn^{III} center, with a Mn–O distance of 2.52 Å. This Mn^{III}–O(H_2O) distance is longer than those determined for the six-coordinate model compound $[(TPP)Mn^{III}(H_2O)_2]ClO_4$ (2.271(2) Å) [66] and the five-coordinate compounds $[(TPP)Mn^{III}(H_2O)]SbF_6$ (2.145(5) Å) [66], $[(TPP)Mn^{III}(H_2O)]OTf$ (2.105(4) Å) [67], and $[(OEP)Mn^{III}(H_2O)]ClO_4$ (2.149(3) Å) [68]. The O-atom of the water ligand in $Mn^{III}Mb(H_2O)$ is 2.62 Å from the N^{ε} atom of the major conformation of the distal His64 residue, indicative of hydrogen-bonding between these moieties. In addition, the O-atom of the coordinated water ligand is tilted 15° from the normal to the heme four-nitrogen (4N) plane towards to the interior of the protein.

The minor (30%) disordered position of the distal water molecule is 3.96 Å from the Mn^{III} center, and is 2.84 Å from the N^{ε} atom of the corresponding minor conformation of the His64 residue; this distance between the water molecule and this distal His64 residue is consistent with hydrogen-bond stabilization of this non-coordinated water in the distal pocket. The Leu29 and Val68 residues are the closest distal pocket moieties to this water molecule; the distance

between the water O-atom and the nearest C-atoms of Leu29 and Val68 are 3.14 and 3.32 Å, respectively. The distance between the O-atom positions of the coordinated and uncoordinated water molecules is 1.70 Å.

We attempted to refine the Mn atom at two positions to correlate with the presence of coordinated and uncoordinated water, but we were not successful. Thus, it is likely that the Mn atom position represents an average between two close-by positions. In the final refined structure, the Mn atom is apically displaced by 0.18 Å from the heme 4N plane towards the proximal His93 residue, with a Mn^{III}–N(His93) distance of 2.22 Å. The displacement of the Mn atom towards the proximal His93 residue is common feature for all the structures reported here (see Table 2), although variations in the extent of the apical displacement are observed depending on the compound being examined.

3.2. $Mn^{III}Mb(ONO^{-})$

We were not able to crystallize this complex from the addition of nitrite to $Mn^{III}Mb(H_2O)$; either by co-crystallization or by soaking of the $Mn^{III}Mb(H_2O)$ crystals with nitrite. Further, we did not observe any spectral change in the Soret region of the UV-vis spectrum upon addition of nitrite to a solution of $Mn^{III}Mb(H_2O)$, consistent with the results from a previous study by Lan *et al.* [43]. However, addition of nitrite to reduced $Mn^{II}Mb$ results in a spectral shift in the UV-vis spectrum from 442 nm to a new "split" Soret peak at 471 and 378 nm indicative of the formation of a new $Mn^{III}Mb$ species. Indeed, we were successful in obtaining crystals of $Mn^{III}Mb(ONO^{-})$ by this method, by adding nitrite to crystals of reduced $Mn^{II}Mb$.

As demonstrated in Fig. 1b, the nitrito (i.e., O-bonded) mode of coordination of the nitrite ligand is present in the $Mn^{III}Mb(ONO)$ complex. The conformation of the Mn–O–N–O moiety is *trans*. The Mn–O(nitrite) bond length is 2.33 Å, and the coordinating O-atom of the nitrite ligand is tilted 10° from the normal to the Mn-heme 4N plane. The Mn–O–N and O–N–O angles are 112° and 119°, respectively. The coordinating atom of the nitrite ligand is 2.57 Å from the N^{ε} atom of the distal His64 residue, indicative of a strong hydrogen-bonding interaction. Further, the nitrite N-atom is 3.3 Å from the His64 N^{ε} atom and the Val68 (nearest C-atom) residues. The terminal O-atom of the nitrite is 3.26 Å from the His64 N^{ε} atom, but is only 3.07 Å from the Leu29 (nearest C-atom) residue. The bond length between the Mn atom and the proximal His93 residue is 2.34 Å, and the Mn atom is displaced by 0.07 Å from the Mn-heme 4N plane towards His93.

3.3. $Co^{III}Mb(H_2O)$

The Co-heme environment in the crystal structure of $Co^{III}Mb(H_2O)$ is shown in Fig. 1c. Selected structural data are shown in Table 2. We note that the 1.65 Å resolution structure for sperm whale $Co^{III}Mb(H_2O)$, (Co–O = 2.19 Å; Co–N(His93) = 2.06 Å; (Co)O···N(His64) = 2.87 Å) has been reported previously [69]. The superposition of the heme environments of horse heart (this work) and sperm whale $Co^{III}Mb(H_2O)$ is shown in Fig. S2 in the Supplementary Information.

3.4. $Co^{III}Mb(ONO^{-})$

Addition of excess nitrite to a solution of $Co^{III}Mb(H_2O)$ results in a 6 nm shift of λ_{max} from 425 nm to 431 nm. This shift is not immediately noticeable (e.g, even after 1 min), but is clearly evident several minutes after mixing of the nitrite and $Co^{III}Mb(H_2O)$ solutions. This 6 nm red-shift is larger than the 3 nm red-shift observed in the reaction of nitrite ion with native *aquomet*Mb (λ_{max} 409 nm) to form Mb(ONO) (λ_{max} 412 nm) [62,70].

Co-crystallization of $Co^{III}Mb(H_2O)$ in the presence of excess sodium nitrite gives crystals of the desired complex with full occupancy of the nitrite ion ligand as determined by

crystallography. Soaking crystals of $Co^{III}Mb(H_2O)$ in a solution containing a high concentration of nitrite for at least 30 min gives the same $Co^{III}Mb(ONO)$ product, but with only ~60% occupancy of the nitrite ligand.

The Co-heme environment of the $Co^{III}Mb(ONO)$ complex obtained from the co-crystallization experiment (with full occupancy of the nitrite ligand) is shown in Fig. 1d. As with the $Mn^{III}Mb(ONO)$ complex described earlier (Fig. 1b), the nitrite ligand displays the nitrito (O-bound) coordination mode with respect to the metal center, and the Co–O–N–O moiety is in a *trans* conformation. The axial Co–O(nitrite) distance is 2.14 Å, and the Co–O–N(nitrite) and O–N–O angles are 105° and 117°, respectively. The coordinating atom of the nitrite ligand is within hydrogen-bonding distance to the N^{ε} atom of the distal His64 residue (at a distance of 2.71 Å), and is tilted by 9° from the normal to the Co-heme 4N plane; the axial (His93)N–Co–O1 bond angle is 173°. The terminal O-atom of the nitrite ligand is situated 3.32 Å from the N^{ε} atom of the distal His64 residue, and is 3.09 and 3.27 Å from the distal Leu29 and Val68 residues, respectively.

3.5. The reduced $Mn^{II}Mb$

Crystals of the reduced $Mn^{II}Mb$ complex were prepared by soaking crystals of $Mn^{III}Mb$ in buffer containing dithionite. The structure of the Mn-heme environment in the resulting $Mn^{II}Mb$ is shown in Fig. 2a. The absence of electron density in the F_o-F_c map was consistent with the absence of an axial water ligand in the distal pocket. Notable features of this structure include a 0.34 Å apical displacement of the Mn atom from the heme 4N plane towards the proximal His93 residue in this five-coordinate compound, with a Mn^{II}–N(His93) distance of 2.27 Å. This is a larger apical displacement of the Mn atom than that observed for the six-coordinate $Mn^{III}Mb(H_2O)$ compound (0.18 Å). The Mn^{II}–N(His93) distance is, however, similar to that in the oxidized $Mn^{III}Mb(H_2O)$ analogue (i.e., only a 0.05 Å difference).

The structure of the heme environment of $Mn^{II}Mb$ reported here has some similarities with the structure of the model five-coordinate compound (TPP)Mn^{II}(1-MeIm) [71]. Both $Mn^{II}Mb$ and (TPP)Mn^{II}(1-MeIm) have a vacant sixth coordination site, with the Mn^{II} centers displaced from the porphyrin 4N planes towards the imidazole groups. In the model compound (TPP)Mn^{II}(1-MeIm), the axial Mn–N(MeIm) bond length is 2.192(2) Å, with the Mn atom apically displaced by 0.51 Å from the four-nitrogen plane of the porphyrin towards the imidazole ligand [71]. Thus, the Mn-N(imidazole) bond length is ~0.08 Å longer in $Mn^{II}Mb$ compared with the related distance in the model complex, and the apical displacement of the Mn atom is 0.16 Å shorter in $Mn^{II}Mb$.

3.6. $Mn^{II}Mb(NO)$

The interaction of NO with reduced $Mn^{II}Mb$ in solution results in a blue shift of the Soret absorption band of $Mn^{II}Mb$ at 442 nm to 429 nm (with β and α bands at 544 and 583 nm, respectively) indicative of the formation of $Mn^{II}Mb(NO)$ [40]. Related absorption bands at (i) 424, 538 and 580 nm,[43] and (ii) 433, 538 and 580 nm [40,72] have been reported for $Mn^{II}Mb(NO)$. For convenience, we will use this oxidation state formalism to describe the adduct formed when NO binds to $Mn^{II}Mb$ (i.e., to distinguish it from the adduct between NO and $Mn^{III}Mb$). We discuss the oxidation state formalism later in the Discussion.

We were not able to obtain, from solution, crystals of the preformed $Mn^{II}Mb(NO)$ complex. Fortunately, soaking crystals of $Mn^{II}Mb$ (obtained by reacting crystals of $Mn^{III}Mb$ with dithionite) with NO also produced the desired nitrosyl product. We determined the 1.9 Å resolution structure of this product, with the NO ligand refining to 70% occupancy. We also located two conformations of the distal His64 residue that refined to 70% and 30% occupancies,

with the major conformation assigned to $Mn^{II}Mb(NO)$, and the minor conformation assigned to $Mn^{II}Mb$. Fig. 2b shows the Mn-heme environment of the crystalline $Mn^{II}Mb(NO)$ product.

The Mn-NO moiety is distinctly bent with a Mn–N–O angle of 130°. The nitrosyl N-atom is tilted by 12° from the normal to the Mn-heme 4N plane, and the NO group is oriented away from the distal His64 residue in the direction of Leu29. The nitrosyl N and O atoms are, respectively, 2.60 and 3.28 Å from the N^{ε} atom of the major conformation of the distal His64 residue, consistent with hydrogen-bonding stabilization of the NO group in the distal pocket. The next closest distance between the NO group and the distal pocket residues is with a carbon atom of Val68 (3.37 Å from the nitrosyl O-atom).

In the structure of this $Mn^{II}Mb(NO)$ complex, the NO ligand refined to 70% occupancy. The apical displacement of Mn by 0.20 Å from the Mn-heme 4N plane towards the proximal His93 residue suggests that the structure shown in Fig. 2b is likely a mixture of $Mn^{II}Mb(NO)$ and $Mn^{II}Mb$ (note that ΔMn for $Mn^{II}Mb$ is 0.34 Å). We were not able to refine the two separate Mn positions, and the rather long Mn–N(O) distance of 2.53 Å may thus not correctly represent this bond length. For comparison, the Mn–N(O) bond length in the model compound (TPP) Mn(NO)(1-MeIm) is 1.641(1) Å [48].

3.7. $Mn^{III}Mb(MeOH)$

As part of a control experiment (see Discussion), we prepared the methanol adduct of $Mn^{III}Mb$ to determine the binding geometry of this ligand. The structure of the Mn^{III}-heme environment is shown in Fig. 2c. The Mn–O(MeOH) bond length is 2.48 Å, which is longer than the analogous Mn–O distance in the d^4 high-spin model non-protein complexes (TPP) $Mn^{III}(N_3)(MeOH)$ (2.329(7) Å) [73], $[(TPP)Mn^{III}(MeOH)_2]ClO_4$ (2.252(2), 2.270(2) Å) [74], and for the five-coordinate $[(OEP)Mn(EtOH)]ClO_4$ (2.145(2) Å) [75].

The major differences between the structure of $Mn^{III}Mb(MeOH)$ and $Mn^{III}Mb(H_2O)$ are (i) only one position of MeOH was found, at full occupancy, (ii) only one His64 conformation was found in $Mn^{III}Mb(MeOH)$, and (iii) the Mn^{III} atom was displaced only 0.07 Å from the heme 4N plane towards the proximal His93 residue. The methyl group of the MeOH ligand is oriented towards the interior of the protein in the direction of the Leu29 and Ile107 amino acid residues; the distance between the C-atom of the MeOH ligand and the nearest carbon atom of the closest residue Val68 is 3.51 Å. The Mn^{III}–O–C(Me) angle of 119° is slightly more acute than that observed in the model compound $[(TPP)Mn^{III}(MeOH)_2]ClO_4$ (124.6(3), 124.0(3)°) [74], perhaps due to the presence of the hydrogen-bonding interaction present in $Mn^{III}Mb(MeOH)$ which might also be responsible for the slightly longer Mn-O bond in the protein.

3.8. $Mn^{III}Mb(N_3^-)$

The azide anion is a known inhibitor of cellular respiration, and it also inhibits the catalytic activities of catalase, cytochrome oxidase, and peroxidases [33]. The azide adduct of Mn-substituted Mb has been characterized by optical and resonance Raman spectroscopy [16,58, 76]. Hoffman and Gibson reported anomalous binding of azide to $Mn^{III}Mb$, and determined that the reaction of azide with $Mn^{III}Mb$ proceeded in two kinetically separable steps to eventually generate $Mn^{III}Mb(N_3^-)$ [35]. In contrast, azide binding to iron-containing *met*Mb is consistent with a single binding equilibrium [77]. The 2.8 Å resolution crystal structure of the azide complex of the iron-containing horse *met*Hb is known [78,79]. The related crystal structure of the azide adduct of *met*Mb was first reported by Stryer *et al.* in 1964 [80]. A comparison of the crystal structures of hh $Mb^{III}(N_3^-)$ (at 2.0 Å resolution) and its His64Thr mutant (at 1.8 Å resolution) was reported by Maurus *et al.* in 1998 [81]. In the wild type adduct, the Fe–N–N(N) bond was 119°, and the Fe–N(azide) bond was 2.11 Å. In the His64Thr mutant structure, two conformations of the azide ligand were present; the major (~90%) conformation

oriented the azide ligand towards the interior of the protein (as seen in the wild type structure), and the minor conformation oriented the azide ligand towards to exterior of the protein towards the solvent. The latter minor conformation is reminiscent of the 1.9 Å resolution crystal structure of the azide adduct of ferric myoglobin isolated from the buccal muscles of the Mediterranean mollusc *Aplysia limacine*, where the azide ligand is oriented towards the solvent [82]; this protein lacks a distal His64(E11) residue.

Given the interest in the conformational preferences of the azide ligand in myglobin, we determined the 1.65 Å resolution crystal structure of hh $Mn^{III}Mb(N_3^-)$. The heme environment is shown in Fig. 2d, and is similar to that of wild type $Mb^{III}(N_3^-)$ [81], in which only one conformation of the azide ligand was observed. In both compounds, the azide ligand is oriented towards the interior of the protein. The Mn^{III}–N(azide) distance of 2.37 Å is longer than those observed in the model complexes (TPP)$Mn^{III}(N_3^-)$(MeOH) (2.176(9) Å) [73], (TPP) $Mn^{III}(N_3^-)$ (2.045 Å) [83], and (Schiff base)$Mn^{III}(N_3^-)$ (2.221(4) Å) [84]. The coordinating atom of the azide ligand is 2.64 Å away from the N^{ε} atom of the distal His64 residue, indicative of a hydrogen-bonding stabilization of the azide ligand in the distal pocket. The next closest nonbonding distance between the azide ligand and distal pocket residues is that between the terminal N3 atom of the azide with the side-chain of Leu29, with an (azide)N-to-Leu(C-atom) distance of 3.46 Å.

As is the case of the iron-containing $Mb^{III}(N_3^-)$, the azide ligand is oriented towards the distal Ile107 residue; other distances between the azide terminal N-atom and non-H atoms of distal pocket residues are with Ile107 (3.55 Å) and Val68 (3.97 Å). The Mn atom in $Mn^{III}Mb(N_3^-)$ is almost in the heme 4N plane, with an apical displacement of only 0.08 Å. The near in-plane position of Mn is consistent with the six-coordination of the metal center and near-complete (94%) occupancy of the azide ligand. The proximal Mn–N(His93) bond length in $Mn^{III}Mb(N_3^-)$ of 2.50 Å is, however, longer than that observed in the iron-containing $Mb^{III}(N_3^-)$ (2.06 Å), demonstrating the effect that the $Mn^{III}d^4$ center has on this axial bond length when compared with the ferric d^5 center. Ferric $Mb^{III}(N_3^-)$ has been shown to exhibit a ground-state low-spin electronic configuration and an observable low-spin/high-spin equilibrium at room temperature [77]. In contrast, the d^4 complex $Mn^{III}Mb(N_3^-)$ is known to be high-spin [35], and this likely accounts for its longer proximal metal–N(His93) bond length.

4. Discussion

The preparation and ligand binding properties of Mn-substituted Mb have been studied in detail by spectroscopic methods. Both Mn^{III}Mb and Mn^{II}Mb are high-spin species [12,14,57,85]. The overall structure of Mn-substituted horse heart Mb is very similar to that of the iron-containing analogue, and the protein retains the typical Mb fold. Maurus *et al.* compared the crystal structures of natural and recombinant wild-type horse heart myoglobin, and showed that small differences existed in the structures [86]. When the final Mn^{III}Mb model is superimposed on the 1.7 Å resolution crystal structure of recombinant horse heart Mb reported by Maurus *et al.* (pdb access code 1WLA) [86], the root-mean square deviations in the backbone and side-chain atomic positions are 0.32 Å and 1.01 Å, respectively. When compared with the structure of natural Mb (pdb access code 1YMB) [87], these values are 0.32 and 1.12 Å, respectively. We find that the structures of the heme environments in our Mn-substituted horse heart myglobins more closely match those of the recombinant iron analogues, particularly with the Leu29 and Val68 side-chain orientations. The superposition of the heme environment structures of $Mn^{III}Mb(H_2O)$ and the two *aquomet*Mb structures are shown in Fig. 3. It is interesting to note that Atassi reported earlier that Mn^{III}Mb and wild-type Mb exhibit identical immunological properties [15].

In this manuscript, we report the crystal structures of the nitrite adducts of Mn- and Co-substituted myoglobin. In addition, we report the structures of the reduced Mn^{II}Mb compound, the nitrosyl product Mn^{II}Mb(NO), and the methanol and azide derivatives of Mn^{III}Mb. Crystals of the parent Mn^{III}Mb were needed for this study, hence we begin by describing the structure of this compound.

4.1. The nature of the heme site in Mn^{III}-substituted myoglobin

Manganese-substituted myoglobin (MnMb) has been prepared and studied in solution for decades. However, the coordination environment around the metal center in MnMb derivatives has been a subject of considerable debate. Mn^{III}Mb displays a characteristic "split" Soret band pattern at λ_{max} 378 and 471 nm, whereas Mn^{II}Mb displays a single Soret peak at λ_{max} 438 nm [12,24,57]. Mitra and coworkers used multinuclear NMR and optical spectroscopy to determine that the sixth axial position in Mn^{III}Mb was unlikely to be occupied by a water molecule [36]. In the latter study, they did not observe a change in the optical spectrum of Mb^{III}Mb in the pH 4–11 range, suggesting the absence of an aquo↔hydroxo equilibrium for a hypothetical axial water ligand. This result differed somewhat from that reported by Spiro and coworkers who studied the resonance Raman spectra of Mn^{III}Mb and found evidence for a weakly interacting axial water ligand in the sixth position [88]. As stated in the Introduction, there is a noticeable paucity of crystal structures of Mn-substituted heme proteins in the literature. Using X-ray difference Fourier techniques, Moffat and coworkers determined that for Mn^{III}Hb, the α hemes contained six-coordinate Mn^{III} centers (with axial water) whereas the β hemes were five-coordinate (i.e., no axial water) [51].

Farmer and coworkers investigated the electrochemical properties of Mn^{III}Mb in dimethyldidodecylammonium bromide surfactant films [89]. They discovered a dynamic exchange between two Mn^{III}/Mn^{II} redox couples ($E_1 = -0.25$ V vs SCE; $E_2 = -0.41$ V vs SCE), and they attributed this to the presence of two forms of Mn^{III}Mb that probably differed in heme site geometry. Interestingly, Hoffman and Gibson reported that Mn^{III}Mb reacted with azide in two kinetically separable steps, and that this was likely due to the presence of two forms of the Mn-porphyrin that differed in the extent of metal displacement from the porphyrin plane [35].

The crystal structure of $Mn^{III}Mb(H_2O)$ reported here sheds new light on this debate regarding the axial coordination geometry of the metal site in this protein. Three independent preparations, crystallizations, and structure solutions at 1.65 Å resolution yielded identical $Mn^{III}Mb(H_2O)$ crystal structures. In the structure, there is a mixture of a six-coordinate species (with axial water; 70% occupancy) and a five-coordinate species (without axial water; a non-bonded water refined to 30% in the distal pocket). We also found two conformations for the distal His64 residue, and these conformations refined to the corresponding 70% and 30% occupancies (Figs. 1a and S1).

During the initial stages of refinement of the structure, we were unsure if the electron density (attributed to an axial ligand) observed in the F_o-F_c difference map was due to an adventitious solvent molecule such as methanol. To test this, we performed the following additional experiments. (i) We effected reduction of the purple-red Mn^{III}Mb crystal with dithionite, and obtained the structure of the resulting orange-red five-coordinate reduced compound Mn^{II}Mb (see later). We then reoxidized this Mn^{II}Mb crystal with ferricyanide and determined its 1.9 Å resolution structure; it was identical to that obtained for $Mn^{III}Mb(H_2O)$ as shown in Fig. 1a. This result reaffirmed to us that the electron density in the distal pocket was not due to an adventitious exogenous ligand such as methanol. (ii) In addition, we prepared the previously unknown methanol adduct by cocrystallizing Mn^{III}Mb in the presence of methanol, and determined the structure of the resulting $Mn^{III}Mb(MeOH)$ product (Fig. 2c, and Results section).

The presence of distal-pocket uncoordinated water in the structure of $Mn^{III}Mb(H_2O)$ is, while initially unexpected, not without precedent in crystal structures of native and mutant iron myoglobins. For example, a similar distal-pocket (non-coordinated) water has been located in the 1.15 Å resolution crystal structures of wild-type ferrous *deoxy*Mb (horse heart and sperm whale), and this water is stabilized by hydrogen-bonding with the distal His64 residue (HOH···N(His) distance of 2.8 Å) [90,91]. In the case of hh *deoxy*Mb, this distal pocket water was located 3.53(5) Å from the Fe center (*c.f.* 2.13 Å for liganded water in *aquomet*Mb) [90]. Further, distal pocket water has been observed in other reported structures of wild-type [92-94] and mutant (V68A [93], V68F [93], V68N (molecule B) [95]) *deoxy*Mb's.

The crystal structure of the Val68Thr mutant of pig *deoxy*Mb provides an interesting comparison with the structure of hh $Mn^{III}Mb(H_2O)$ reported here. In molecule A of the Val68Thr *deoxy*Mb, a single water molecule is distributed between two positions; one position is within direct bonding distance to Fe (Fe–O = 1.9 Å; 30% occupancy of H_2O), and the other is positioned 3.5 Å from the Fe (70% occupancy of H_2O) yet within hydrogen-bonding distance of the distal His64 residue (HOH··· N^{ε}(His) = 2.6 Å) [96]. In molecule B, a single position of the distal water located 3Å from Fe is observed, and this is also within hydrogen-bonding distance to the His64 residue (HOH···N^{ε}His) = 2.6 Å) [96].

The distance between the two distal pocket water molecule positions in $Mn^{III}Mb(H_2O)$ is 1.70 Å. This distance is inconsistent with the presence of a dioxygen ligand (*c.f.*, the O–O distance of 1.24 Å in *oxy*Mb) [90], as are the refined occupancies of the O atoms. Further, this 1.70 Å distance is too short for a HOH···OH_2 hydrogen-bonding interaction, and rules out the presence of both coordinated and unligated H_2O in the same molecule (such presence of coordinated and uncoordinated H_2O has been observed in the 1.9 Å resolution structure of native sw *aquomet*Mb) [92].

The location of the distal pocket (non-coordinated) water molecule in $Mn^{III}Mb(H_2O)$ is reminiscent of the distal docking site for photodissociated CO from MbCO as determined by X-ray crystallography [97-99]. For example, the crystal structure of photolyzed hh MbCO shows the CO ligand in a position that is 3.6 Å from the Fe atom and atop a carbon pyrrole [97]. This site is in the general area as, but not the same as, the distal pocket Xe binding site (i.e., the Xe_4 site) [100].

Importantly, the displacement of the distal pocket water in *deoxy*Mb has been linked to the kinetic barriers for CO binding to ferrous Mb [92,101]. It is thus likely that the presence of two types of distal H_2O in $Mn^{III}Mb(H_2O)$ (i.e., coordinated and uncoordinated) helps explain the presence of two Mn^{III}/Mn^{II} redox couples for the electrochemical reduction of $Mn^{III}Mb$ [89] and the two kinetically separable steps for the reaction of azide with $Mn^{III}Mb$ [35]. Finally, we note that Moffat and coworkers have utilized X-ray difference Fourier techniques to determine that the Mn center in the α-heme of $Mn^{III}Hb$ binds H_2O as a sixth ligand, whereas the β-heme does not and is five-coordinate [51].

4.2. The nitrite complexes of $Mn^{III}Mb$ and $Co^{III}Mb$

There is renewed interest in the nature of binding of the nitrite anion to heme proteins [102-106]. It has long been appreciated that the direct heme-nitrite interaction is an essential one insofar as nitrite reduction by the heme-containing nitrite reductases (NiRs) is concerned. Nitrite is reduced to NO by the NiRs [107-109], and this process is believed to involve initial binding of nitrite directly to the iron center in the heme-containing NiRs.

To date, the reported crystal structures of the nitrite adducts of heme-containing NiRs and related compounds all display N-binding of the nitrite ligand. For example, the crystal structure

of the nitrite adduct of cytochrome cd_1 NiR from *P. Pantotrophus* reveals the N-binding (i.e., nitro) mode of nitrite to the iron center [110].

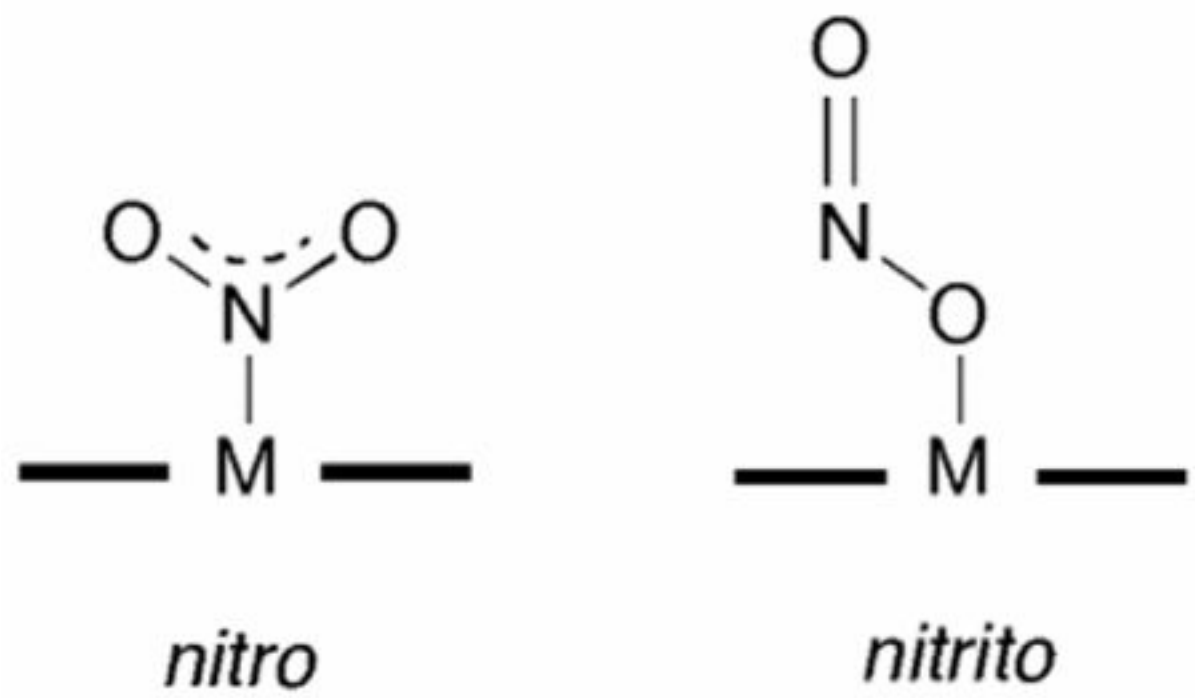

This nitrite adduct was obtained by soaking crystals of ferrous NiR with nitrite, it is reasonable to assume that such an N-binding mode would facilitate protonation of a nitrite terminal O-atom to result in eventual release of NO and a water molecule. The crystal structure of the nitrite adduct of *ferric* cytochrome *c* NiR from *Wolinella succinogenes* also shows N-binding of the nitrite anion to the iron center, and density functional calculations on the related *model* compound (por)$Fe^{III}(NH_3)(NO_2)$ reveals that the N-binding mode is more stable than the nitrito O-binding mode by >10 kcal/mol [111]. The crystal structure of the nitrite adduct of the sulfite reductase hemoprotein from *E. coli* similarly reveals an N-binding mode of the nitrite anion to the iron center [112].

Interestingly, DFT calculations on the nitrite adduct of cytochrome cd_1 NiR provide intriguing possibilities for nitrite coordination to the heme center in this enzyme [113]. Although the nitrito O-binding mode was determined to be 4.5 kcal/mol higher in energy than the corresponding nitro N-binding mode in the ferric form (6 kcal/mol in the ferrous form), the nitrito form was considered to also be a viable intermediate in NiR catalysis.

The nitro N-binding mode has been determined for all crystallographically characterized synthetic iron porphyrins containing the nitrite ligand, regardless of whether the iron center is formally in the ferric or ferrous state [114]. The only exception to this is that for the nitrite in the anionic complex $[(TpivPP)Fe(NO)(NO_2)]^-$ which displays both N-binding (nitro) and O-binding (nitrito) of the disordered nitrite group [115]. Results of DFT calculations on a model iron porphyrin with NO and nitrite ligands show that the nitrito linkage isomer (porphine)Fe(NO)(ONO) is only 4.3 kcal/mol higher in energy than the related nitro isomer (porphine)Fe(NO)(NO_2) [116].

We recently reported the 1.3 Å resolution X-ray crystal structure of the nitrite adduct of ferric horse heart Mb, and determined that the nitrite anion was bound to the ferric center via the

nitrito O-binding mode [62]. Importantly, this structure was the first to demonstrate *that a stable O-binding mode of nitrite is possible in heme proteins*. Given this rather unexpected nitrito binding mode for the nitrite ligand in the iron-containing d^5 compound $Mb^{III}(ONO^-)$ and the role of the distal pocket in stabilizing this (to date) unusual binding mode, we sought to investigate the nitrite binding preferences within the distal pockets of the d^4 Mn^{III} and d^6 Co^{III} analogues.

To the best of our knowledge, there is only one report of a crystal structure of a synthetic manganese porphyrin containing nitrite, namely that of $(TPP)Mn^{III}(ONO^-)$ [117]. This compound clearly reveals a nitrito O-binding mode of the nitrite anion. Interestingly, although continuous photolysis of this compound shows the formation of (TPP)Mn(O) and NO [117, 118], flash photolysis studies on this compound reveal dissociation of NO_2 from the metal center [119]. Recombination of NO_2 with the $(TPP)Mn^{II}$ photoproduct then proceeds via a nitro $(TPP)Mn(NO_2)$ intermediate that isomerizes to the more stable (TPP)Mn(ONO) compound [119]. Not surprisingly, therefore, the crystal structure of $Mn^{III}Mb(ONO^-)$ also shows that the nitrite anion binds to the manganese center via the nitrito O-binding mode (Fig. 2b).

Our crystallography results for the nitrite adduct of cobalt-substituted myoglobin was unexpected, however. To date, all crystallographically characterized nitrite adducts of synthetic cobalt porphyrins demonstrate that the nitrite anion is bound to the cobalt centers via the nitro N-binding mode [120-123]. To the best of our knowledge, there is no exception to this observation for model cobalt porphyrin compounds. Indeed, it was demonstrated that during the recombination of NO_2 with $(TPP)Co^{II}$ (generated from flash photolysis of $(TPP)Co^{III}(NO_2)$), an intermediate forms which decays to $(TPP)Co^{III}(NO_2)$; the intermediate was assigned as the nitrito linkage isomer $(TPP)Co^{III}(ONO)$ [124].

To the best of our knowledge, no nitrite adducts of cobalt-substituted heme proteins or related cobalt biomolecules have been characterized. Thus, the structure of $Co^{III}Mb(ONO^-)$ represents the first report of a cobalt nitrite heme protein, and is the first stable nitrito binding to cobalt porphyrins to be established. Clearly, it is evident that although information from crystal structures of cobalt nitrite compounds of model porphyrins have helped in understanding the mechanisms of action of these compounds as catalysts for chemical transformation such as O-atom transfers in oxidation reactions (generating (por)Co(NO) intermediates) [123], the structures may not correlate very well with the geometries present in cobalt-substituted heme proteins. The ability of the distal pocket in $Co^{III}Mb$ to effect the nitrito O-binding preference is significant, and suggests that the hydrogen-bonding provided by the distal His64 residue plays a primary role in stabilizing this binding mode. Since such a moderate-to-strong hydrogen bonding capability is absent in most synthetic cobalt porphyrins with nitrite ligands, it is thus not surprising that this O-binding mode has yet to be observed in these model compounds. It is somewhat surprising, however, that even in the picket fence porphyrin derivatives such as $(TpivPP)Co(NO_2)(1\text{-MeIm})$ which provide electrostatic interactions between “distal” NH groups and bound nitrite, that this stabilization is not sufficient to induce O-binding of the nitrite group [121], perhaps due to the artificial symmetrical nature of the distal pockets.

In summary, the X-ray crystal structures reported to date of synthetic Mn, Fe, and Co porphryins with nitrite ligands reveal a preference for nitrito O-binding for the Mn compound, and nitro N-binding for the Fe and Co compounds. In the Mb derivatives, however, all three metal-nitrite derivatives (Mn^{III}, Fe^{III}, and Co^{III}) reveal the nitrito O-binding mode, suggesting that the distal pocket of Mb is the major determinant in this structural preference for these Mb nitrite derivatives. This observation provides evidence that the O-binding mode of nitrite is not exempt from involvement in nitrite reduction to NO. This is further demonstrated by the

successful reduction of the $Mn^{III}Mb(ONO^{-})$ (this work) and $Mb^{III}(ONO^{-})$ [62] by dithionite to their NO-derivatives.

In the next two sections, we discuss the crystal structures of the dithionite-reduced compound $Mn^{II}Mb$ and its NO derivative.

4.3. The structure of the reduced $Mn^{II}Mb$ complex

The reduction of $Mn^{III}Mb$ to $Mn^{II}Mb$ in solution is a well-studied reaction, and the reduction can be effected using dithionite [16,57,76], radiolysis [57], or electrochemical methods employing surfactant films [89] or employing the mediator oxazine-170 perchlorate [125]. Hori *et al.* employed powder and single-crystal multifrequency EPR spectroscopy to determine that the metal center in $Mn^{II}Mb$ is high-spin $3d^5$ ($S = 5/2$) [85], and this is consistent with a singly-occupied strongly antibonding $d_{x^2-y^2}$ orbital [12]. Arnone and coworkers reported the 3.0 Å resolution crystal structure of the metallohybrid hemoglobin Hb(α-$Fe^{II}CO$)(β-Mn^{II}) that crystallizes in the *deoxy*Hb T-state [53]. They determined that the β-Mn^{II} subunit is structurally isomorphous with the normal *deoxy* β-Fe subunit.

The crystal structure of $Mn^{II}Mb$ reported here reveals that the distal pocket water molecules of $Mn^{III}Mb(H_2O)$ are displaced upon dithionite reduction. Thus, unlike the case of $Mn^{III}Mb(H_2O)$, no water molecules were located in the vicinity of the Mn^{II} center. This contrasts with several reported crystal structures of iron-containing *deoxy*Mb where a non-coordinated water molecule has been located in the distal pocket [90-94,126].

The apical displacement of the Mn atom in $Mn^{II}Mb$ (ΔMn = 0.34 Å) from the heme 4N plane is larger than that observed for $Mn^{III}Mb(H_2O)$ (ΔMn = 0.18 Å). This increase in apical displacement upon reduction of the protein is similar to that seen in the high-resolution structures of reduced Mb (ΔFe = 0.363(11) Å) vs. *aquomet*Mb (ΔFe = 0.106(7) Å) [90]. The heme environments of $Mn^{III}Mb(H_2O)$ and $Mn^{II}Mb$, obtained from the overlay of the protein C_α backbones, are shown in Fig. 4. Differences are evident in the water ligation and distal His64 placement in these proteins. The His64 residue in the reduced $Mn^{II}Mb$ more closely overlaps the minor conformation of the His64 residue in $Mn^{II}Mb(H_2O)$. Fig. S3 shows an overlay of the heme sites in the reduced $Mn^{II}Mb$ and *deoxy*Mb ($Fe^{II}Mb$, Fig. S3). In the reduced $Fe^{II}Mb$ case, one of the two conformations of the distal His64 residue reveals an inward movement that supposedly helps stabilize the distal pocket water molecule through hydrogen-bonding, whereas in the reduced $Mn^{II}Mb$ case such a hydrogen-bond stabilization is not present due to the lack of distal pocket water.

4.4. The nitric oxide complex

For convenience, the nitrosyl adduct of $Mn^{II}Mb$ is represented as $Mn^{II}Mb(NO)$, although it is perhaps better represented as $\{MnNO\}^6$ (see later). In order to place the NO ligand conformation observed in $Mn^{II}Mb(NO)$ in proper context, some discussion of formalism is warranted [127,128]. For example, the oxidation state formalism has often been used to describe metal nitrosyl linkages. In this formalism, NO binding to a metal center (M) to generate a linear M-NO unit results in a complex formulated as $M^{-}(NO^{+})$, where a formal electron transfer to the metal has occurred. Conversely, when a bent M-NO moiety is generated, the complex is formulated as $M^{+}(NO^{-})$. Clearly, this formalism is overly simplistic. Although it does take into account that NO is a redox active ligand, it does not account for cases where the unpaired electron density on NO essentially still resides on the ligand in its metal complex. Enemark and Feltham developed a notation that treats the metal-NO fragment as a single unit, and the use of the resulting formalism avoids the oxidation state simplification of the metal-NO group [129-131]. In this $\{MNO\}^n$ formalism, n denotes the number of assigned electrons to the metal *d* orbitals (without consideration of the NO ligand(s)) plus an electron for each of

the attached NO ligands. Thus, the (por)Mn(NO) complex belongs to the $\{MnNO\}^6$ class, and the (por)Fe(NO) belongs to the $\{MNO\}^7$ class. According to this formalism as applied to nitrosyl metallopophyrins, $\{MNO\}^6$ compounds have preferred linear NO geometries, and $\{MNO\}^7$ compounds have bent (~145°) NO geometries. In synthetic six-coordinate iron nitrosyl porphyrins of the $\{MNO\}^7$ class, the FeNO angles are in the tight 137–140° range (avg. ~138.5°) [114,132]. A much wider range of FeNO bond angles (112°–160°) is observed in nitrosyl heme proteins, however [62]. We reported the 1.3 Å resolution crystal structures of hh MbNO, and showed that two reproducible FeNO angles (~144° and 120°) are obtained depending on the method of preparation of the complex [62]. The variability of FeNO angle in the heme pocket of MbNO had been demonstrated previously by Hori *et al.* using single crystal EPR spectroscopy; the FeNO angle was 153 ± 5 at 293K, but was 109 ± 5 at 77 K [133]. Chien and Dickenson showed, using single crystal EPR spectroscopy, that the FeNO angles in $Hb_K NO$ were 167° in the α-subunits and 105° in the β-subunits [41]. It is thus likely that subtle distal pocket effects influence the metal-NO bond geometry in nitrosyl adducts of heme proteins. We now consider the case of $Mn^{II}Mb(NO)$ and compare the observed geometry to that expected from synthetic manganese nitrosyl porphyrins.

To date, all synthetic (por)Mn(NO)-containing compounds of the $\{MnNO\}^6$ class (i.e., $Mn^{II}NO$) that have been characterized by X-ray crystallography display linear Mn-NO groups [48,49,134,135]. The expected and observed linearity of the MnNO bonds is supported by the spectroscopic characterization of several low-spin (por)Mn(NO)-containing compounds [44, 46,128,136]. Yu *et al.* employed resonance Raman spectroscopy to demonstrate that steric constraints within the distal face of a synthetic "strapped" (por)Mn(NO) complex enhances the Mn–N–O bending mode, and they attributed this observation to a tilting of the *trans* Mn–N (*N*-base) bond [136].

As stated in the Introduction, NO adducts of Mn-substituted heme proteins have been prepared and characterized by spectroscopy. $Mn^{III}Mb$ does not bind NO, however $Mn^{II}Mb$ does [40]. Interestingly, Gersonde and coworkers demonstrated, using resonance Raman spectroscopy, that the monomeric $Mn^{III}Hb$ compound from the insect *Chironomus thummi thummi* binds NO to give the $Mn^{III}NO$ adduct, but this undergoes autoreduction to the $Mn^{II}NO$ derivative [42].

To the best of our knowledge, the crystal structure of $Mn^{II}Mb(NO)$ reported in this work (Fig. 2b) represents the first distinctly bent MnNO moiety in a natural or synthetic manganese heme complex. The NO ligand refines to 70% occupancy, but the MnNO bend is clearly evident in the structure. The nitrosyl N atom is 2.6 Å away from the N^{ε} atom of the major conformation of the distal His64 residue, suggesting strong hydrogen-bond stabilization of the NO molecule in the distal pocket. As mentioned in the Results section, the observed long Mn–NO distance of 2.53 Å is likely an average distance that has contributions from the unligated five-coordinate $Mn^{II}Mb$ complex and the nitrosyl adduct. Assuming that the Mn atom were in the heme 4N plane in $Mn^{II}Mb(NO)$, the resulting Mn–NO distance would still be rather long. Thus, we propose that the geometry of the MnNO moiety observed here represents that of a loosely bound NO molecule to the metal center that is held in place by strong hydrogen-bonding to the distal His64 residue. This geometry is also likely determined by the method of preparation of the complex, namely the nitrosylation of the *preformed* distal pocket in the $Mn^{II}Mb$ crystals. Such a procedure may disfavor linear (strong) binding of the NO ligand without significant movement of the distal His64 residue away from its position in $Mn^{II}Mb$. We are continuing attempts to crystallize pre-formed $Mn^{II}Mb(NO)$ to test this hypothesis.

Supplementary Material

Refer to Web version on PubMed Central for supplementary material.

Acknowledgments

The authors are grateful to the National Institutes of Health (GM 64476; GBR-A) for funding for this research. ZNZ thanks the Government of Egypt for a Ph.D. scholarship.

References

1. Percy MJ, McFerran NV, Lappin TRJ. Blood Reviews 2005;19:61–68. [PubMed: 15603910]
2. Chui JS, Poon WT, Chan KC, Chan AY, Buckley TA. Anaesthesia 2005;60:496–500. [PubMed: 15819771]
3. Gladwin MT, Schechter AN, Kim-Shapiro DB, Patel RP, Hogg N, Shiva S, Cannon RO III, Kelm M, Wink DA, Espey MG, Oldfield EH, Pluta RM, Freeman BA, Lancaster JR Jr, Feelisch M, Lundberg JO. Nat Chem Biol 2005;1:308–314. [PubMed: 16408064]and references therein2006;2(2): 110.Erratum:
4. Bryan NS. Free Rad Biol Med 2006;41:691–701. [PubMed: 16895789]
5. Cosby K, Partovi KS, Crawford JH, Patel RP, Reiter CD, Martyr S, Yang BK, Waclawiw MA, Zalos G, Xu X, Huang KT, Shields M, Kim-Shapiro DB, Schechter AN, Cannon RO III, Gladwin MT. Nat Med 2003;9:1498–1505. [PubMed: 14595407]
6. Hunter CJ, Dejam A, Blood AB, Shields H, Kim-Shapiro DB, Machado RF, Tarekegn S, Mulla N, Hopper AO, Schecter AN, Power GG, Gladwin MT. Nat Med 2004;10:1122–1127. [PubMed: 15361865]
7. Doyle MP, Pickering RA, DeWeert TM, Hoekstra JW, Pater D. J Biol Chem 1981;256:12393–12398. [PubMed: 7298665]
8. Nagababu E, Ramasamy S, Abernethy DR, Rifkind JM. J Biol Chem 2003;278:46349–46356. [PubMed: 12952953]
9. Grubina R, Huang A, Shiva S, Joshi MS, Azarov I, Basu S, Ringwood LA, Jiang A, Hogg N, Kim-Shapiro DB, Gladwin MT. J Biol Chem 2007;282:12916–12927. [PubMed: 17322300]
10. Samouilov A, Kuppusamy P, Zweier JL. Arch Biochem Biophys 1998;357:1–7. [PubMed: 9721176]
11. Shiva S, Huang Z, Grubina R, Sun J, Ringwood LA, MacArthur PH, Xu X, Murphy E, Darley-Usmar VM, Gladwin MT. Cir Res 2007;100:654–661.
12. Boucher LJ. Coord Chem Rev 1972;7:289–329.
13. Fabry TL, Simo C, Javaherian K. Biochim Biophys Acta 1968;160:118–122. [PubMed: 5651687]
14. Yonetani T, Drott HR, Leigh JS Jr, Reed GH, Waterman MR, Asakura T. J Biol Chem 1970;245:2998–3003. [PubMed: 4317879]
15. Atassi MZ. Biochem J 1967;103:29–35. [PubMed: 6068005]
16. Yonetani T, Asakura T. J Biol Chem 1969;244:4580–4588. [PubMed: 4309145]
17. Breslow E. J Biol Chem 1964;239:486–496. [PubMed: 14169149]
18. Gelb MH, Toscano WA Jr, Sligar SG. Proc Natl Acad Sci USA 1982;79:5758–5762. [PubMed: 6964386]
19. Dierks EA, Hu S, Vogel KM, Yu AE, Spiro TG, Burstyn JN. J Am Chem Soc 1997;119:7316–7323.
20. Dickinson LC, Chien JCW. J Biol Chem 1977;252:6156–6162. [PubMed: 19468]
21. Hemmens B, Gorren ACF, Schmidt K, Werner ER, Mayer B. Biochem J 1998;332:337–342. [PubMed: 9601061]
22. Theorell H. Nature (London) 1945;156:474.
23. Ozols J, Strittmatter P. J Biol Chem 1964;239:1018–1023. [PubMed: 14167616]
24. Yonetani T. J Biol Chem 1967;242:5008–5013. [PubMed: 6058943]
25. Yonetani T, Asakura T. J Biol Chem 1968;243:3996–3998. [PubMed: 4298518]
26. Gupta K, Selinsky BS, Loll PJ. Acta Cryst 2006;D62:151–156.
27. Borg DC, Cotzias GC. Nature 1958;182:1677–1678. [PubMed: 13622617]
28. Borg DC, Cotzias GC. Fed Proc 1959;18:470.
29. Mahoney JP, Sargent K. J Clin Invest 1967;46:1090.
30. Hancock RGV, Fritze K. Bioinorg Chem 1973;3:77–87.

31. Wibowo AAE, Salle HJA, del Castiho P, Zielhuis RL. Int Arch Occup Environ Health 1979;43:177–182. [PubMed: 457290]
32. Baden SP, Neil DM. Comp Biochem Physiol A: Mol Integr Physiol 1998;119A:351–359. [PubMed: 11253807]
33. Keilin D. Proc Roy Soc B 1936;121:165–173.
34. Hoffman BM, Gibson QH, Bull C, Crepeau RH, Edelstein SJ, Fisher RG, McDonald MJ. Ann N Y Acad Sci 1975;244:174–186. [PubMed: 1056162]
35. Hoffman BM, Gibson QH. Biochemistry 1976;15:3405–3410. [PubMed: 952865]
36. Mondal MS, Mazumdar S, Mitra S. Inorg Chem 1993;32:5362–5367.
37. Gibson QH, Hoffman BM, Crepeau RH, Edelstein SJ, Bull C. Biochem Biophys Res Commun 1974;59:146–151. [PubMed: 4842296]
38. Bull C, Fisher RG, Hoffman BM. Biochem Biophys Res Commun 1974;59:140–145. [PubMed: 4858350]
39. Gibson QH, Hoffman BM. J Biol Chem 1979;254:4691–4697. [PubMed: 438210]
40. Yonetani T, Yamamoto H, Erman JE, Leigh JJS, Reed GH. J Biol Chem 1972;247:2447–2455. [PubMed: 4336375]
41. Chien JCW, Dickinson LC. J Biol Chem 1977;252:1331–1335. [PubMed: 190230]
42. Lin SH, Yu NT, Gersonde K. FEBS Lett 1988;229:367–371. [PubMed: 3345847]
43. Lan EH, Dave BC, Fukuto JM, Dunn B, Zink JI, Valentine JS. J Mater Chem 1999;9:45–53.
44. Wayland BB, Olson LW. Inorg Chim Acta 1974;11:L23–L24.
45. Wayland BB, Olson LW, Siddiqui ZU. J Am Chem Soc 1976;98:94–98.
46. Piciulo PL, Scheidt WR. Inorg Nucl Chem Lett 1975;11:309–311.
47. Kelly S, Lançon D, Kadish KM. Inorg Chem 1984;23:1451–1458.
48. Zahran ZN, Shaw MJ, Khan MA, Richter-Addo GB. Inorg Chem 2006;45:2661–2668. [PubMed: 16529489]
49. Zahran ZN, Lee J, Alguindigue SS, Khan MA, Richter-Addo GB. Dalton Trans 2004:44–50. [PubMed: 15356740]
50. Yu CH, Su YO. J Electroanal Chem 1994;368:323–327.
51. Moffat K, Loe RS, Hoffman BM. J Mol Biol 1976;104:669–685. [PubMed: 950673]
52. Moffat K, Loe RS, Hoffman BM. J Am Chem Soc 1974;96:5259–5261. [PubMed: 4851221]
53. Arnone A, Rogers P, Blough NV, McGourty JL, Hoffman BM. J Mol Biol 1986;188:693–706. [PubMed: 3735432]
54. Makino R, Matsuda H, Obayashi E, Shiro Y, Iizuka T, Hori H. J Biol Chem 1999;274:7714–7723. [PubMed: 10075661]
55. Teale FWJ. Biochim Biophys Acta 1959;35:543. [PubMed: 13837237]
56. Yonetani T, Yamamoto H, Woodrow GV III. J Biol Chem 1974;249:682–690. [PubMed: 4855813]
57. Langley R, Hambright P, Alston K. Inorg Chem 1986;25:114–117.
58. Yu NT, Tsubaki M. Biochemistry 1980;19:4647–4653. [PubMed: 7426622]
59. Pflugrath J. Acta Crystallogr 1999;D55:1718–1725.
60. Project C. Acta Crystallogr 1994;D50:760–763.
61. Vagin A, Teplyakov A. J Appl Crystallogr 1997;30:1022–1025.
62. Copeland DM, Soares A, West AH, Richter-Addo GB. J Inorg Biochem 2006;100:1413–1425. [PubMed: 16777231]
63. Arendall WB III, Tempel W, Richardson JS, Zhou W, Wang S, Davis IW, Liu ZJ, Rose JP, Carson WM, Luo M, Richardson DC, Wang BC. J Struct Funct Genomics 2005;6:1–11. [PubMed: 15965733]
64. Davis IW, Murray LW, Richardson JS, Richardson DC. Nucl Acids Res 2004;32:W615–W619. [PubMed: 15215462]Web Server
65. Brunger AT, Adams PD, Clore GM, DeLano WL, Gros P, Grosse-Kunstleve RW, Jiang JS, Kuszewski J, Nilges M, Pannu NS, Reed RJ, Rice LM, Simonson T, Warren GL. Acta Crystallogr 1998;D54:905–921.

66. Williamson MM, Hill CL. Inorg Chem 1987;26:4155–4160.
67. Williamson MM, Hill CL. Inorg Chem 1986;25:4668–4671.
68. Cheng B, Cukiernik F, Fries PH, Marchon JC, Scheidt WR. Inorg Chem 1995;34:4627–4639.
69. Brucker EA, Olson JS, Phillips GN Jr, Dou Y, Ikeda-Saito M. J Biol Chem 1996;271:25419–25422. [PubMed: 8810310]
70. Sono M, Dawson JH. J Biol Chem 1982;257:5496–5502. [PubMed: 6279603]and references therein
71. Kirner JF, Reed CA, Scheidt WR. J Am Chem Soc 1977;99:2557–2563. [PubMed: 850028]
72. Parthasarathi N, Spiro TG. Inorg Chem 1987;26:2280–2282.
73. Day VW, Stults BR, Tasset EL, Day RO, Marianelli RS. J Am Chem Soc 1974;96:2650–2652. [PubMed: 4833718]
74. Hatano K, Anzai K, Iitaka Y. Bull Chem Soc Jpn 1983;56:422–427.
75. Cheng B, Scheidt WR. Acta Crystallogr 1996;C52:585–588.
76. Cox RP, Hollaway MR. Eur J Biochem 1977;74:575–587. [PubMed: 856586]
77. Bogumil R, Hunter CL, Maurus R, Tang HL, Lee H, Lloyd E, Brayer GD, Smith M, Mauk AG. Biochemistry 1994;33:7600–7608. [PubMed: 8011626]
78. Perutz MF, Mathews FS. J Mol Biol 1966;21:199–202. [PubMed: 5969763]
79. Deatherage JF, Obendorf SK, Moffat K. J Mol Biol 1979;134:419–429. [PubMed: 537070]
80. Stryer L, Kendrew JC, Watson HC. J Mol Biol 1964;8:96–104. [PubMed: 14149967]
81. Maurus R, Bogumi B, Nguyen NT, Mauk AG, Brayer G. Biochem J 1998;322:67–74. [PubMed: 9576852]
82. Mattevi A, Gatti G, Coda A, Rizzi M, Ascenzi P, Brunori M, Bolognesi M. J Mol Recogn 1991;4:1–6.
83. Day VW, Stults BR, Tasset EL, Marianelli RS. Inorg Nucl Chem Lett 1975;11:505–509.
84. Brooker S, McKee V. Acta Cryst 1993;C49:441–445.
85. Hori H, Ikeda-Saito M, Reed GH, Yonetani T. J Magn Reson 1984;58:177–185.
86. Maurus R, Overall CM, Bogumi R, Luo Y, Mauk AG, Smith M, Brayer GD. Biochem Biophys Acta 1997;1341:1–13. [PubMed: 9300804]
87. Evans SV, Brayer GD. J Mol Biol 1990;213:885–897. [PubMed: 2359126]
88. Parthasarathi N, Spiro TG. Inorg Chem 1987;26:3792–3796.
89. Lin R, Immoos CE, Farmer PJ. J Biol Inorg Chem 2000;5:738–747. [PubMed: 11129001]
90. Vojtechovsky J, Chu K, Berendzen J, Sweet RM, Schlichting I. Biophys J 1999;77:2153–2174. [PubMed: 10512835]
91. Kachalova GS, Popov AN, Bartunik HD. Science 1999;284:473–476. [PubMed: 10205052]
92. Quillin ML, Arduini RM, Olson JS, Philips GN Jr. J Mol Biol 1993;234:140–155. [PubMed: 8230194]
93. Quillin ML, Li T, Olson JS, Phillips GN Jr, Y D, Ikeda-Saito M, Regan R, Carlson M, Gibson QH, Li H, Elber R. J Mol Biol 1995;245:416–436. [PubMed: 7837273]
94. Takano T. J Mol Biol 1977;110:569–584. [PubMed: 845960]
95. Krzywda S, Murshudov GN, Brzozowksi AM, Jaskolski M, Scott EE, Klizas SA, Gibson QH, Olson JS, Wilkinson AJ. Biochemistry 1998;37:15896–15907. [PubMed: 9843395]
96. Cameron AD, Smerdon SJ, Wilkinson AJ, Habash J, Helliwell JR, Li T, Olson JS. Biochemistry 1993;32:13061–13070. [PubMed: 8241160]
97. Chu K, Vojtchovsky J, McMahon BH, Sweet RM, Berendzen J, Schlichting I. Nature 2000;403:921–923. [PubMed: 10706294]
98. Schotte F, Soman J, Olson JS, Wulff M, Anfinrud PA. J Struct Biol 2004;147:235–246. [PubMed: 15450293]
99. Nienhaus GU, Nienhaus K. J Biol Phys 2002;28:163–172.
100. Brunori M, Bourgeois D, Vallone B. J Struct Biol 2004;147:223–234. [PubMed: 15450292]
101. Springer BA, Sligar SG, Olson JS, Phillips GN Jr. Chem Rev 1994;94:699–714.
102. Huang Z, Shiva S, Kim-Shapiro DB, Patel RP, Ringwood LA, Irby CE, Huang KT, Ho C, Hogg N, Schechter AN, Gladwin MT. J Clin Invest 2005;115:2099–2107. [PubMed: 16041407]
103. Gladwin MT. Nat Chem Biol 2005;1:245–246. [PubMed: 16408049]

104. Kim-Shapiro DB, Gladwin MT, Patel RP, Hogg N. J Inorg Biochem 2005;99:237–246. [PubMed: 15598504]
105. Huang KT, Keszler A, Patel N, Patel RP, Gladwin MT, Kim-Shapiro DB, Hogg N. J Biol Chem 2005;280:31126–31131. [PubMed: 15837788]
106. Duranski MR, Greer JJM, Dejam A, Jaganmohan S, Hogg N, Langston W, Patel RP, Yet SF, Wang X, Kevil CG, Gladwin MT, Lefer DJ. J Clin Invest 2005;115:1232–1240. [PubMed: 15841216]
107. Averill BA. Chem Rev 1996;96:2951–2964. [PubMed: 11848847]
108. Hollocher, TC. The Enzymology and Occurrence of Nitric Oxide in the Biological Nitrogen Cycle. In: Lancaster, J., editor. Nitric Oxide Principles and Applications. Academic Press; San Diego: 1996. p. 289-344.
109. Eady, RR.; Hasnain, SS. Denitrification. In: Que, L., Jr; Tolman, WB., editors. Comprehensive Coordination Chemistry II. Elsevier; San Diego, CA: 2004. p. 759-786.
110. Williams PA, Fulop V, Garman EF, Saunders NFW, Ferguson SJ, Hajdu J. Nature 1997;389:406–412. [PubMed: 9311786]
111. Einsle O, Messerschmidt A, Huber R, Kroneck PMH, Neese F. J Am Chem Soc 2002;124:11737–11745. [PubMed: 12296741]
112. Crane BR, Siegel LM, Getzoff ED. Biochemistry 1997;36:12120–12137. [PubMed: 9315849]
113. Silaghi-Dumitrescu R. Inorg Chem 2004;43:3715–3718. [PubMed: 15180427]
114. Wyllie GRA, Scheidt WR. Chem Rev 2002;102:1067–1089. [PubMed: 11942787]
115. Nasri H, Ellison MK, Chen S, Huynh BH, Scheidt WR. J Am Chem Soc 1997;119:6274–6283.
116. Novozhilova IV, Coppens P, Lee J, Richter-Addo GB, Bagley KA. J Am Chem Soc 2006;128:2093–2104. [PubMed: 16464112]
117. Suslick KS, Watson RA. Inorg Chem 1991;30:912–919.
118. Suslick KS, Watson RA. New J Chem 1992;16:633–642.
119. Hoshino M, Nagashima Y, Seki H, Leo MD, Ford PC. Inorg Chem 1998;37:2464–2469.
120. Yamamoto K, Iitaka Y. Chem Lett 1989:697–698.
121. Jene PG, Ibers JA. Inorg Chem 2000;39:3823–3827. [PubMed: 11196776]
122. Adachi H, Suzuki H, Miyazaki Y, Iimura Y, Hoshino M. Inorg Chem 2002;41:2518–2524. [PubMed: 11978120]
123. Goodwin J, Kurtikyan T, Standard J, Walsh R, Zheng B, Parmley D, Howard J, Green S, Mardyukov A, Przybla DE. Inorg Chem 2005;44:2215–2223. [PubMed: 15792456]
124. Seki H, Okada K, Iimura Y, Hoshino M. J Phys Chem A 1997;101:8174–8178.
125. Taniguchi I, Li CZ, Ishida M, Yao Q. J Electroanal Chem 1999;460:245–250.
126. Nienhaus K, Ostermann A, Nienhaus GU, Parak FG, Schmidt M. Biochemistry 2005;44:5095–5105. [PubMed: 15794647]
127. Richter-Addo, GB.; Legzdins, P. Metal Nitrosyls. Oxford University Press; New York: 1992.
128. Cheng, L.; Richter-Addo, GB. Binding and Activation of Nitric Oxide by Metalloporphyrins and Heme. In: Guilard, R.; Smith, K.; Kadish, KM., editors. The Porphyrin Handbook. Vol. 4. Academic Press; New York: 2000. p. 219-291.
129. Feltham RD, Enemark JH. Top Stereochem 1981;12:155–215.
130. Westcott, BL.; Enemark, JH. Transition Metal Nitrosyls. In: Lever, ABP.; Solomon, EI., editors. Inorganic Electronic Structure and Spectroscopy. Vol. Chapter 7. Wiley and Sons; New York: 1999.
131. Enemark JH, Feltham RD. Coord Chem Rev 1974;13:339–406.
132. Wyllie GRA, Schultz CE, Scheidt WR. Inorg Chem 2003;42:5722–5734. [PubMed: 12950223]
133. Hori H, Ikeda-Saito M, Yonetani T. J Biol Chem 1981;256:7849–7855. [PubMed: 6267028]
134. Scheidt WR, Hatano K, Rupprecht GA, Piciulo PL. Inorg Chem 1979;18:292–299.
135. Piciulo PL, Rupprecht G, Scheidt WR. J Am Chem Soc 1974;96:5293–5295.
136. Yu NT, Lin SH, Chang CK, Gersonde K. Biophys J 1989;55:1137–1144. [PubMed: 2765651]

5. Abbreviations

C*c*P
: cytochrome *c* peroxidase

DFT
: density functional theory

Hb_k
: hemoglobin Kansas

hh
: horse heart

1-MeIm
: 1-methylimidazole

Mb
: myoglobin

NiR
: nitrite reductase

OEP
: dianion of 2,3,7,8,12,13,17,18-octaethylporphyrin

OTf
: triflate anion

PGHS
: prostaglandin H_2 synthase

por
: porphyrinato dianion

PPIX
: dianion of protoporphyrin IX

SCE
: saturated calomel electrode

sGC
: soluble guanyly cyclase

sw
: sperm whale

TPP
: dianion of 5,10,15,20-tetraphenylporphyrin

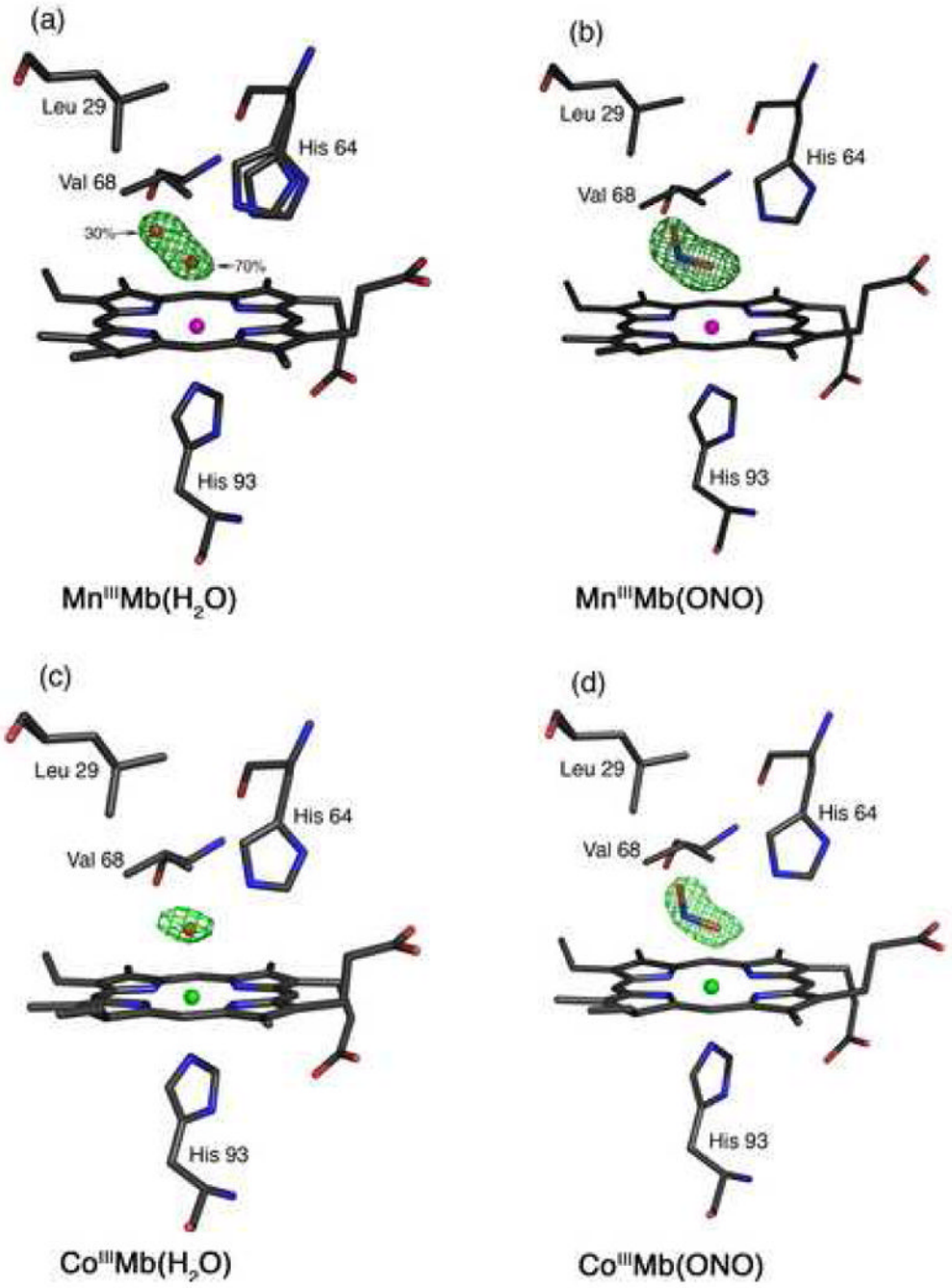

Fig. 1.

Final models and final F_o-F_c difference electron density maps showing side views of hh MnMb and CoMb derivatives. Carbon, oxygen, nitrogen, Mn and Co atoms are colored grey, red, blue, magenta and green, respectively. The bonds to Mn and Co are not shown for clarity. (a) $Mn^{III}Mb(H_2O)$: The difference electron density map contoured at 3σ shows a single water molecule in two different positions. (b) $Mn^{III}Mb(ONO)$: The difference electron density map contoured at 2.5σ. (c) $Co^{II}Mb(H_2O)$: The difference electron density map contoured at 2.5σ. (d) $Co^{III}Mb(ONO)$: The difference electron density map contoured at 2.5σ.

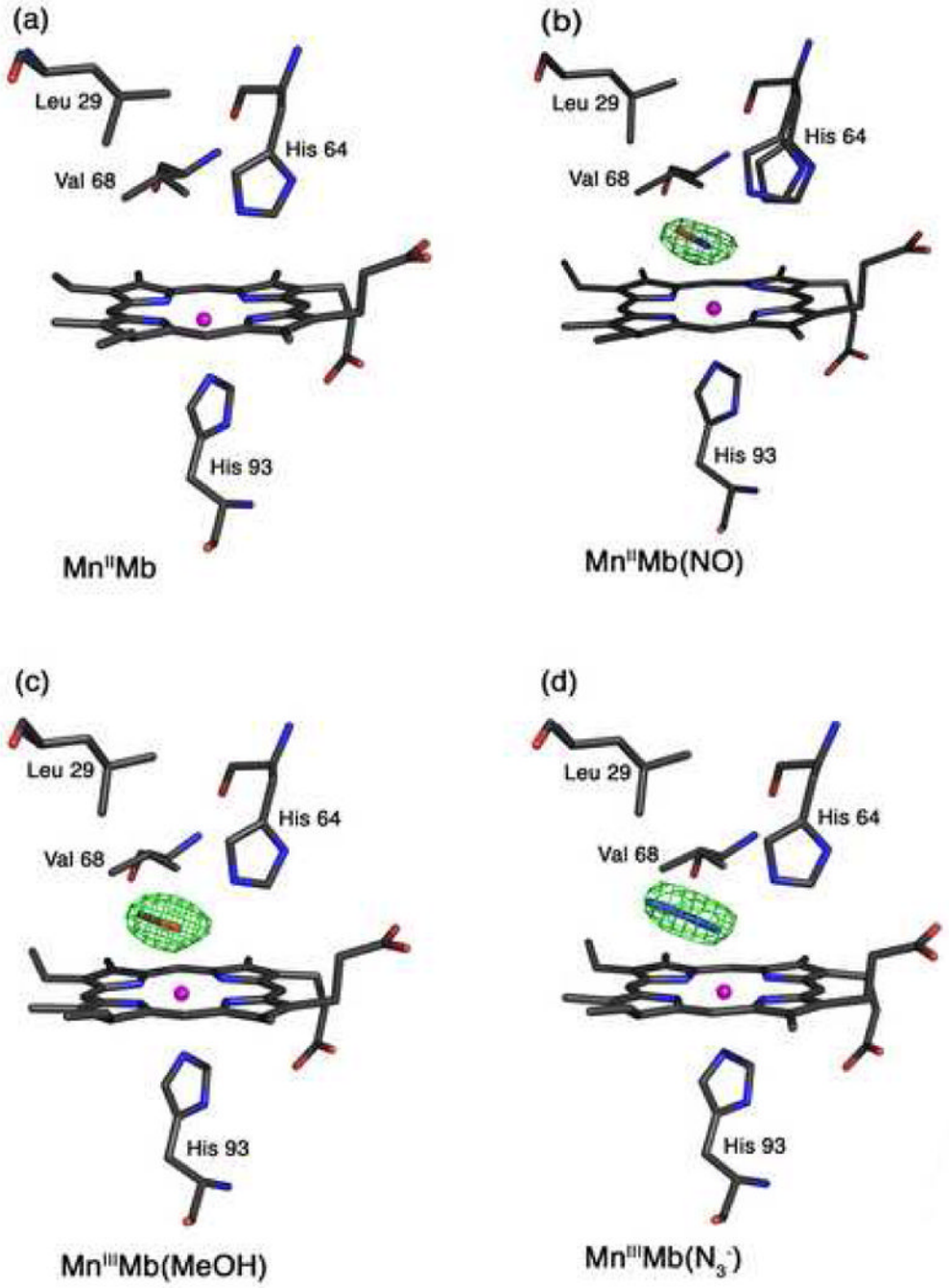

Fig. 2.

Final models and final F_o-F_c difference electron density maps showing side views of hh MnMb and CoMb derivatives. Carbon, oxygen, nitrogen, Mn, and Co atoms are colored grey, red, blue, magenta, and green, respectively. The bonds to Mn and Co are not shown for clarity. (a) The reduced $Mn^{II}Mb$ showing the absence of electron density for a coordinated water molecule in the active site. (b) $Mn^{II}Mb(NO)$: The difference electron density map contoured at 3σ shows an NO molecule that refined to 70% occupancy. (c) $Mn^{III}Mb(ONO)$: The difference electron density map is contoured at 3σ. (d) $Mn^{III}Mb(N_3^-)$: The difference electron density map is contoured at 3σ.

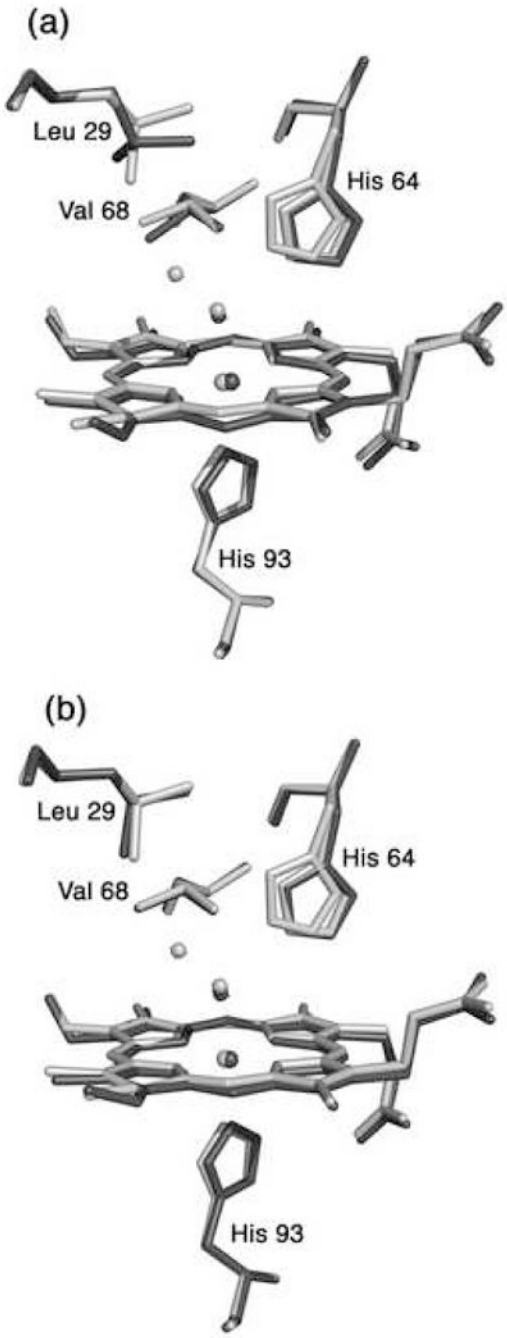

Fig. 3.

A superposition of the heme environments in the crystal structures of hh $Mn^{III}Mb(H_2O)$ (this work, shown in light grey) and (a) natural hh $Fe^{III}Mb(H_2O)$ (pdb code 1YMB [80], shown in dark grey), and (b) recombinant hh $Fe^{III}Mb(H_2O)$ (pdb code 1WLA [79], shown in dark grey), using a global Cα structural alignment. The major conformation of His64 in hh $Mn^{III}Mb(H_2O)$ is similar to the conformation in $Fe^{III}Mb(H_2O)$. The Leu29 and Val68 conformations of the Mn- and Fe-proteins overlay better in the structures shown in Fig. 3b.

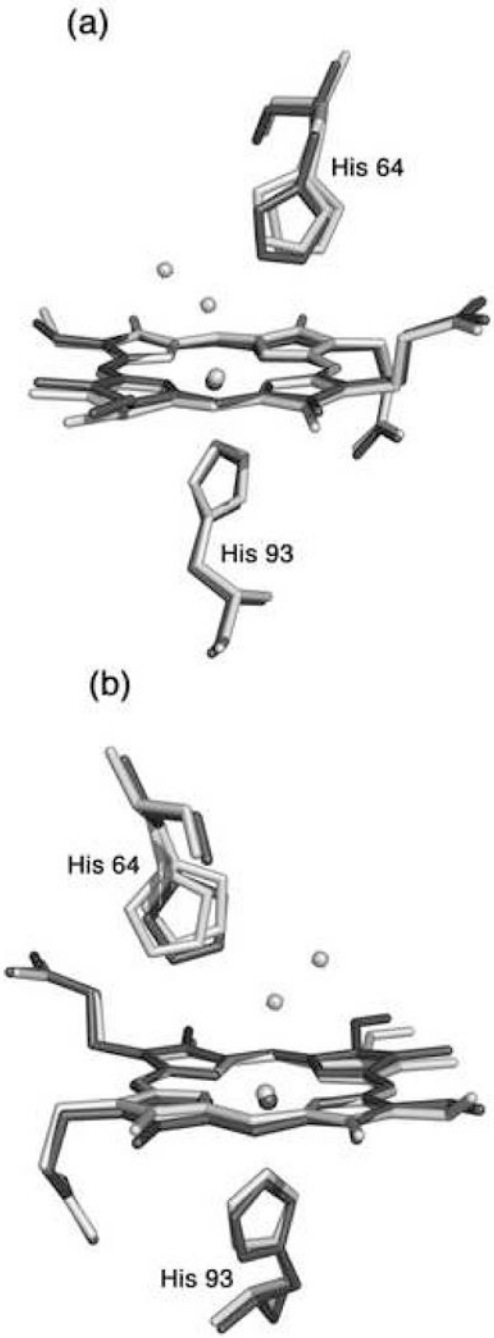

Fig. 4.

A superposition of the heme environments in the crystal structures of hh $Mn^{III}Mb(H_2O)$ (this work, shown in light grey) and hh $Mn^{II}Mb$ (this work, shown in dark grey) using a global Cα structural alignment, and shown from two different views. The N^{ε} atoms of the His64 and His93 residues of $Mn^{II}Mb$ are shifted from their major/minor positions in $Mn^{III}Mb(H_2O)$ by 0.95/0.21 and 0.37 Å, respectively. Also, the Mn^{II} center is shifted 0.25 Å from its Mn^{III} position. A *meso* carbon and its connecting pyrrole ring A are shifted towards the proximal side in $Mn^{II}Mb$ relative to those in $Mn^{III}Mb(H_2O)$.

Table 1

Statistics of X-Ray data collection and refinement

	$Mn^{III}Mb(H_2O)$	$Mn^{III}Mb(ONO)$	$Co^{III}Mb(H_2O)$	$Co^{III}Mb(ONO)$	$Mn^{II}Mb$	$Mn^{II}Mb(NO)$	$Mn^{III}Mb(MeOH)$	$Mn^{III}Mb(N_3)$
PDB code	2O58	2O5O	2O5T	2O5S	2O5B	2O5Q	2O5L	2O5M
Data collection [a]								
Space group	$P2_1$	$P2_1$	$P2_1$	$P2_1$	$P2_1$	$P2_1$	$P2_1$	$P2_1$
Cell Dimen.								
a (Å)	35.41	35.43	35.31	35.17	35.21	35.47	35.41	35.48
b (Å)	28.65	28.67	28.75	28.68	28.74	28.64	28.59	28.75
c (Å)	62.94	62.99	63.03	63.36	64.20	63.19	63.20	62.91
β (°)	106.0	105.5	106.5	106.1	105.45	105.7	105.74	105.9
Resolution (Å)	1.65	1.60	1.60	1.60	2.00	1.90	1.70	1.65
Mean $I/\sigma(I)$	15.2 (4.4)	14.5 (4.0)	10.1 (2.9)	20.4 (4.7)	9 (2.7)	9.0 (2.5)	12.5 (3.9)	17.0 (4.6)
No. Reflections								
Observed	63842	68845	64903	65732	25281	35301	58562	64306
Unique	14874	16177	15721	15758	8510	9669	13275	14301
Comp. (%)	99.6 (98.2)	98.5 (95.9)	96.2 (87.2)	96.5 (86.6)	98.7 (96.0)	97.8 (99.9)	96.8 (93.7)	95.3 (91.0)
R_{merge} (%)[b]	5.6 (26.4)	5.3 (31.6)	7.7 (34.8)	4.4 (16.8)	7.6 (31.8)	9.5 (23.6)	6.8 (36.4)	5.1 (27.2)
Refinement								
Res. Range (Å)	19.47-1.65	25.92-1.60	26.51-1.60	26.58-1.60	20.63-2.00	26.57-1.90	21.91-1.70	26.75-1.65
R-factor (%)[c]	17.9	18.6	19.3	17.4	19.4	17.7	17.4	18.4
R_{free} (%)[d]	22.3	22.4	24.8	21.5	23.9	21.8	23.3	22.1
rmsd bond dist.	0.015	0.013	0.017	0.012	0.023	0.021	0.014	0.015
rmsd angles (°)	1.57	2.26	2.47	2.28	2.05	2.49	1.53	2.29
B factor ($Å^2$)								
Mean	17.6	16.88	21.59	15.36	32.12	22.02	18.17	16.2
rmsd main	0.82	0.81	0.85	0.77	1.15	1.05	0.86	0.81
rmsd side	2.4	2.27	2.49	2.37	3.06	2.80	2.48	2.34

[a] Values in parentheses correspond to the highest resolution shells for $Mn^{III}Mb(H_2O)$ (1.71–1.65 Å), $Mn^{III}Mb(ONO)$ (1.66–1.60 Å), $Co^{III}Mb(H_2O)$ (1.66–1.60 Å), $Co^{III}Mb(ONO)$ (1.66–1.60 Å), $Mn^{II}Mb$ (2.07-2.00), $Mn^{II}Mb(NO)$ (1.97–1.90 Å), $Mn^{III}Mb(MeOH)$ (1.76–1.70 Å), and $Mn^{III}Mb(N_3^-)$ (1.71–1.65 Å).

[b] $R_{merge} = \Sigma|I - \langle I \rangle|/\Sigma(I)$ where I is the individual intensity observation and $\langle I \rangle$ is the mean of all measurements of I.

[c] R-factor $= \Sigma||F_O| - |F_C||/\Sigma|F_O|$ where F_O and F_C are the observed and calculated structure factors, respectively.

[d] R_{free} is calculated using randomly selected reflections comprising 5% of the data not used throughout refinement.

Table 2

Selected geometrical data for the Mn- and Co-substituted myoglobin complexes.

Compound	M–N(por) (Å)	M–X(axial)[a] (Å)	M-X-Y (°)	α (°)[b]	M–N(His93)	(M)X···N(His64)[c] (Å)	ΔM[d] (Å)
$Mn^{III}Mb(H_2O)$	2.04-2.08	2.52[e]	–	15.3[e]	2.22	2.62[e]	−0.18
$Mn^{III}Mb(ONO^-)$	2.02-2.10	2.33	112	9.7	2.34	2.57	−0.07
$Co^{III}Mb(H_2O)$	2.02-2.09	2.46	–	11.7	2.15	2.54	−0.04
$Co^{III}Mb(ONO^-)$	2.06-2.07	2.14	105	8.8	2.02	2.71	−0.04
$Mn^{II}Mb$	2.03-2.10	–	–	–	2.27	–	−0.34
$Mn^{II}Mb(NO)$[f]	2.06-2.11	2.53[f]	130	12.5	2.20[f]	2.60	−0.20[f]
$Mn^{III}Mb(MeOH)$	2.02-2.07	2.48	119	8.2	2.29	2.56	−0.07
$Mn^{II}Mb(N_3^-)$	2.04-2.06	2.37	121	8.9	2.50	2.64	−0.08

[a] Distance between the metal and the coordinating atom of the ligand in the distal pocket.

[b] Tilt of the coordinating atom X (of the distal ligand) from the normal to the heme 4N plane.

[c] Distance between the coordinating atom X (of the distal ligand) and the nearest N-atom of the distal His64 residue.

[d] Apical displacement of the central metal atom from the heme 4N plane towards the distal ligand.

[e] These data are for the component with coordinated H_2O (70% occupancy).

[f] The NO ligand refined to 70% occupancy. Hence, these data likely represent an average of the $Mn^{II}Mb$ (30%) and $Mn^{II}Mb(NO)$ (70%) components (see text). The hydrogen bonding distance to the distal His64 residue is for the major His64 component.